# ELASTIC WAVE PROPAGATION IN IRREGULAR STRUCTURES

Thesis by

Tai-Lin Hong

In Partial Fulfillment of the Requirements
for the Degree of
Doctor of Philosophy

California Institute of Technology
Pasadena, California

1978

(Submitted May 22, 1978)

# ACKNOWLEDGEMENTS

I am grateful to my thesis adviser, Donald V. Helmberger. During my four years of residence in Caltech,his guidance has made me feel that the search for truth is a pleasure.

I appreciate Dan Kosloff for introducing me to the finite element method of analysis and for providing me with many codes which he developed or modified.

I wish to thank my teachers in Caltech, especially Wolfgang Knauss, Hiroo Kanamori, David Harkrider, Thomas Hughes, Julius Miklowitz, Eli Sternberg for broadening my views and motivating my thoughts.

I have benefited from discussions with Thomas Heaton, David Cole, Robert Geller, David Hadley, George Mellman, Charles Langston, Larry Burdick and many other members of the Seismological Laboratory.

A special word of appreciation goes to Leon Teng, who first brought me to the field of seismology and showed continuing interest in my progress later on. I also wish to thank my teachers at the University of Southern California, especially Gregory Davis and John Nodvik.

Financial support for this research,which came from ONR under contract N00014-76-C-1070, NSF under grant ENV 76-10506, and AFOSR under contract 49620-77-C-0022, is sincerely appreciated.

I thank Laszlo Lenches for his help in preparing many difficult figures. I thank Marla Turner for typing the manuscript. The operators and consultants of Booth Computing Center are appreciated for numerous services. ERDA and Caltech high energy physics group are acknowledged for allowing me to use their CDC-7600 computer and remote terminal facilities.

# ABSTRACT

Wave propagation problems involving irregular structures rarely have exact solutions. However,the most important features of such problems can be often obtained from appropriate approximate solutions.

In Chapter 1, we consider refraction problems involving dipping layers. The Cagniard-de Hoop method for flat structures is extended to such problems to evaluate the non-geometric effects of critical reflection and tunneling. It is shown that the character of the dispersion is strongly affected by even relatively shallow angle dips.

In Chapter 2, we consider teleseismic problems involving curved interfaces. An approximation theory, which we name "Glorified Optics", is developed to evaluate the effects of focusing and triplication due to the local curvature along such interfaces. Seismograms are dramatically complicated by those interference effects. The correlation between such complexity and the subsurface structure can be explicitly conceived through Glorified Optics.

In Chapter 3, we perform an independent check on these approximation theories by using finite element methods. The excellent agreement confirms the validity of our approximations.

The concepts,methods and results presented in this thesis appear to be helpful in opening a new dimension in the fields of seismic modelling,inversion and prospecting.

# TABLE OF CONTENTS

# INTRODUCTION

Irregular structures,such as corrugated surfaces, dipping nonconformities, alluvial basins, continental margins, subduction slabs, intrusions and petroleum reservoirs are common features in the earth's crust and upper mantle. Thus wave propagation in such structures is a very important subject in seismology.

There are two types of problems in which we are interested.

1. Refraction problems, in which each individual phase can be highly dispersed due to the non-geometric effects, e.g. critical reflection and tunneling. The Cagniard-de Hoop method is very efficient in evaluating those effects for flat layered structures. In Chapter 1, we extend this method to the cases involving dipping interfaces, by introducing certain approximations.

2. Teleseismic problems, in which we can assume the travel time is infinitely large compared to the source duration. In structures involving curved interfaces, although it is still true that each individual phase will not be significantly dispersed,the overall shape of the seismogram can become very complicated due to the effects of focusing and triplication. In Chapter 2, we develop the "Glorified Optics" method to evaluate such effects.

In Chapter 3, we design efficient grid systems for a finite element code, with which we run a series of numerical experiments to check the validity of the previous approximations.

# Chapter 1

# GENERALIZED RAY THEORY FOR DIPPING STRUCTURE

## ABSTRACT

In this study we relax the strong limiting condition of parallel layering which is usually assumed in seismic modeling by allowing dipping boundaries. We start with the derivation of generalized ray theory in a wedge-shaped medium with free and rigid boundaries. Then, through the development of the method of equivalent models and de-Hoop contours, we extend the theory to dipping structure with elastic boundaries. The effect of a dipping interface over a halfspace for the case of a line source is shown by a series of numerical models which include various angles of dip and source-to-receiver distances. Results for a line source situated below the layer indicate that, when the layer thickens toward the receiver, one obtains a waveform similar to the case where the source is actually in the layer. These features are produced by the combination of forward and backward traveling rays which can have super critical reflections.

# INTRODUCTION

The seismologist can find it difficult to apply elasticity theory to seismic wave problems for many reasons. One difficulty often encountered is that physical constitution parameters have depth dependences. This problem has been handled in many ways, one of which is by approximating the earth structure by a stack of homogeneous layers and applying the concepts of generalized ray theory. Although horizontally layered models have proven useful in many situations, one is constantly confronted with non-horizontal structures where the usual analytical methods are not applicable. Rather than relying on relatively expensive numerical techniques to study these types of problems, it would be useful to develop analytical approximations which can provide some insight along with the solution. We will discuss one such approximate technique for the treatment of wave motion in locally dipping structure in this study.

We introduce the method by considering an SH-line source in a wedge shaped medium with a free surface and a rigid lower boundary. After applying the classical ray expansion, as discussed by Hudson (1963), we solve for the motion by application of the Cagniard-de Hoop technique. A localized coordinate system is adopted which conserves the de Hoop contour and can be easily modified to include elastic boundaries. We are therefore able to recover not only optical results but head waves and tunnelling effects as well. Unfortunately, we can not determine the accuracy of this procedure since there is no other analytical work available to do an independent check, but a comparison of our results with those of finite element methods, which will be shown in Fig. 3.3, is in general good.

# THEORY

Hudson (1963) presented the analytical solution for SH wave propagation in a wedge with one side free and the other side rigid. Here, before introducing our approximate theory,we would like to examine this problem through Cagniard-de Hoop method.

We assume a line source situated in a wedge as diagramed in Figure 1.1. The equation of motion in terms of displacement for a whole space containing this source is simply:

$$\nabla^2 \overline{W}_0 - \frac{s^2}{\beta^2} \overline{W}_0 = \frac{\delta(R)}{R} \cdot \frac{-\overline{f}(s)}{2\pi} \tag{1.1}$$

where "-" denotes the Laplace transform , s in the Laplace variable, $W_0$ is the SH-displacement, and f(t) is the source time function.

By setting $\overline{f}(s) = 2\pi$, we have

$$\overline{W}_0 = K_0(\rho R) \tag{1.2}$$

where $\rho = s/\beta$, and $K_0$ is the modified Bessel function of order zero. Following the transformation by Oberhettinger (1954), we obtain

$$\overline{W}_0 = -i \int_{-\infty}^{\infty} I_{-i\lambda}(\rho r') \cdot K_{i\lambda}(\rho r) \cdot \frac{\cosh\left[\lambda(\pi - |\theta - \theta'|)\right]}{\sinh \pi\lambda} \, d\lambda \tag{1.3}$$

The homogeneous solution is assumed to have the following form

$$\overline{W}_r = -i \int_{-\infty}^{\infty} I_{-i\lambda}(\rho r') \cdot K_{i\lambda}(\rho r) \cdot \left[f_1(\lambda)\, e^{\lambda\theta} + f_2(\lambda)\, e^{-\lambda\theta}\right] d\lambda \tag{1.4}$$

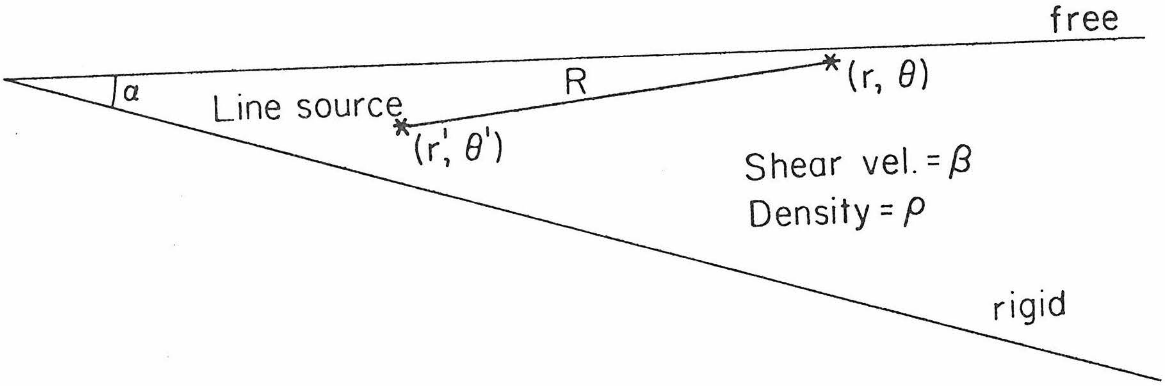

Figure 1.1 Diagram of the problem setup with θ measured clockwise from the free surface. The distances from the tip of the wedge to the source and receiver are r' and r with the separation given as R .

The functions $f_1(\lambda)$ and $f_2(\lambda)$ are to be determined by the following boundary conditions

$$\begin{aligned} \frac{\partial \overline{W}}{\partial \theta} &= 0, \text{ at } \theta = 0 \\ \text{and } \overline{W} &= 0, \text{ at } \theta = \alpha \end{aligned} \qquad (1.5)$$

where, $\overline{W} = \overline{W}_0 + \overline{W}_r$

We obtain,

$$\begin{aligned} f_1 &= \frac{-\sinh[\lambda(\pi-\theta')]e^{-\lambda\alpha} - \cosh[\lambda(\pi-\alpha+\theta')]}{2\cosh(\lambda\alpha)\sinh(\lambda\pi)} \\ f_2 &= \frac{-\cosh[\lambda(\pi-\alpha+\theta')]+\sinh[\lambda(\pi-\theta')]e^{\lambda\alpha}}{2\cosh(\lambda\alpha)\sinh(\lambda\pi)} \end{aligned} \qquad (1.6)$$

Thus at a receiver with $\theta = 0$, we have

$$\overline{W} = -i \int_{-\infty}^{\infty} I_{-i\lambda}(\rho r') \cdot K_{i\lambda}(\rho r) \cdot \frac{2\sinh\lambda(\alpha-\theta')}{\cosh(\lambda\alpha)}\, d\lambda \qquad (1.7)$$

For short period pulses we use the classical approximation (Erdelyi, et al., 1953).

$$\begin{aligned} I_{-i\lambda}(\rho r') &= \frac{e^{\xi'}}{\sqrt{2\pi}\,[(\rho r')^2 - \lambda^2]^{\frac{1}{4}}}\,[1 + O(\lambda^{-1})] \\ K_{i\lambda}(\rho r) &= \frac{e^{-\xi}}{\sqrt{2/\pi}\,[(\rho r)^2 - \lambda^2]^{\frac{1}{4}}}\,[1 + O(\lambda^{-1})] \end{aligned} \qquad (1.8)$$

where,

$$\xi' = [(\rho r')^2 - \lambda^2]^{\frac{1}{2}} + \lambda \sin^{-1}(\lambda/\rho r')$$

$$\xi = [(\rho r)^2 - \lambda^2]^{\frac{1}{2}} + \lambda \sin^{-1}(\lambda/\rho r)$$

Thus we get

$$\overline{W} \simeq -i \int_{-\infty}^{\infty} \frac{e^{\xi'-\xi}}{[(\rho r')^2 - \lambda^2]^{\frac{1}{4}}[(\rho r)^2 - \lambda^2]^{\frac{1}{4}}} \; \frac{\sinh[\lambda(\alpha-\theta')]}{\cosh \lambda\alpha} \, d\lambda$$

$$\simeq -i \int_{-i\infty}^{i\infty} \frac{e^{\xi'-\xi}}{[(\rho r')^2 - \lambda^2]^{\frac{1}{4}}[(\rho r)^2 - \lambda^2]^{\frac{1}{4}}} \left\{ \sum_{n=0}^{N_1} (-1)^n e^{-\lambda\theta'-2n\alpha\lambda} \right.$$

$$+ \sum_{n=1}^{N_2} (-1)^n e^{\lambda\theta'-2n\alpha\lambda} + \frac{(-1)^{N_1+1} \cosh[\lambda\pi-\lambda\theta'-(2N_1+1)\alpha\lambda]}{2 \sinh \lambda\pi \cosh \lambda\alpha}$$

$$\left. + \frac{(-1)^{N_2+1} \cosh[\lambda\pi+\lambda\theta'-(2N_2+1)\alpha\lambda]}{2 \sinh \lambda\pi \cosh \lambda\alpha} \right\} d\lambda \qquad (1.9)$$

where $N_1$, $N_2$ are the largest positive integers to keep $\theta'+2N_1\alpha<\pi$ and $-\theta'+2N_2\alpha<\pi$.

We distorted the integral path to the imaginary axis and by using the principle of Schwarz reflection we obtain

$$\overline{W} \simeq 2 \,\mathrm{Im} \left\{ \sum_{n=0}^{N_1} \int_0^{i\infty} (-1)^n \frac{e^{-s(\phi+\theta'\gamma+2n\alpha\gamma)}}{[(r'/\beta)^2 - \gamma^2]^{\frac{1}{4}}\,[(r/\beta)^2-\gamma^2]^{\frac{1}{4}}} \, d\gamma \right.$$

$$+ \sum_{n=1}^{N_2} \int_0^{i\infty} (-1)^n \frac{e^{-s(\phi-\theta'\gamma+2n\alpha\gamma)}}{[(r'/\beta)^2 - \gamma^2]^{\frac{1}{4}}\,[(r/\beta)^2-\gamma^2]^{\frac{1}{4}}} \, d\gamma$$

$$+\int_0^{i\infty} \frac{(-1)^{N_1+1}\; e^{-s\phi}\; \cosh[s\gamma\pi - s\gamma\theta' - s\gamma(2N_1+1)\alpha]}{2\sinh(s\gamma\pi\,)\;\cosh(s\gamma\alpha)\;[(r'/\beta)^2-\gamma^2]^{\frac{1}{4}}[(r/\beta)^2-\gamma^2]^{\frac{1}{4}}}\,d\gamma$$

$$+\int_0^{i\infty} \frac{(-1)^{N_2+1}\; e^{-s\phi}\; \cosh[s\gamma\pi + s\gamma\theta' - s\gamma(2N_2+1)\alpha]}{2\sinh(s\gamma\pi)\;\cosh(s\gamma\alpha)\;[(r'/\beta)^2-\gamma^2]^{\frac{1}{4}}[(r/\beta)^2-\gamma^2]^{\frac{1}{4}}}\,d\gamma \Bigg\} \qquad (1.10)$$

Where,

$$\gamma = \lambda/s$$

$$\phi = [(r/\beta)^2-\gamma^2]^{\frac{1}{2}} - [(r'/\beta)^2-\gamma^2]^{\frac{1}{2}} + \gamma\sin^{-1}(\gamma\beta/r) - \gamma\sin^{-1}(\gamma\beta/r')$$

The first two terms are the summations of multiples trapped between the two boundaries. The other two terms are the diffracted waves from the wedge tip, which we will neglect for reasons which will become apparent later.

Then by Cagniard-de Hoop method we have

$$W \overset{\sim}{=} \sum_{n=1}^{N} W_n = \sum_{n=1}^{N} \operatorname{Im}\left\{ \frac{2\,\mathcal{R}_n}{\left[\left(\frac{r'}{\beta}\right)^2-\gamma^2\right]^{\frac{1}{4}}\left[\left(\frac{r}{\beta}\right)^2-\gamma^2\right]^{\frac{1}{4}}}\;\frac{d\gamma}{dt}\right\}_{\Gamma_n} \qquad (1.11)$$

where $\Gamma_n$ is the contour in the complex $\gamma$-plane defined by

$$\begin{aligned} &\phi+\theta'\gamma+(n-1)\alpha\gamma = \text{pure real, if } n = \text{odd} \\ &\phi-\theta'\gamma+(n)\alpha\gamma = \text{pure real, if } n = \text{even} \end{aligned} \qquad (1.12)$$

and,

$$N = N_1 + N_2 + 1$$
$$\mathcal{R}_n = (-1)^{n-1}$$

The factor $(2\mathcal{R}_n)$ is the reflection effect, $\mathcal{R}_n$ is the product of all reflection coefficients which are either 1 at the free surface or (-1) at the rigid boundary. The factor 2 is the free surface effect, and the factor

$$\frac{\frac{d\gamma}{dt}}{\left[\left(\frac{r'}{\beta}\right)^2-\gamma^2\right]^{\frac{1}{4}}\left[\left(\frac{r}{\beta}\right)-\gamma^2\right]^{\frac{1}{4}}}$$

controls the spreading effect.

Next, we illustrate the behavior of these generalized rays by examining the first motion approximation of a particular ray diagramed in Figure 1.2, with

$$t(\gamma) = \left[\left(\frac{r}{\beta}\right)^2-\gamma^2\right]^{\frac{1}{2}} - \left[\left(\frac{r'}{\beta}\right)^2-\gamma^2\right]^{\frac{1}{2}} + \gamma\sin^{-1}\left(\frac{\gamma\beta}{r}\right) - \gamma\sin^{-1}\left(\frac{\gamma\beta}{r'}\right) + (2\alpha-\theta')\,\gamma \tag{1.13}$$

The geometric time, $t_0$, is obtained by setting $\frac{\partial t}{\partial \gamma} = 0$ and solving for appropriate $\gamma_0$,

$$\frac{dt}{d\gamma} = (2\alpha-\theta') + \sin^{-1}\left(\frac{\gamma\beta}{r}\right) - \sin^{-1}\left(\frac{\gamma\beta}{r'}\right) \tag{1.14}$$

But since $\varepsilon'-\varepsilon = 2\alpha - \theta'$ one obtains

$$\gamma_0 = \frac{r'\sin\varepsilon'}{\beta} = \frac{r\sin\varepsilon}{\beta} \tag{1.15}$$

Substituting $\gamma_0$ into (1.13) one obtains

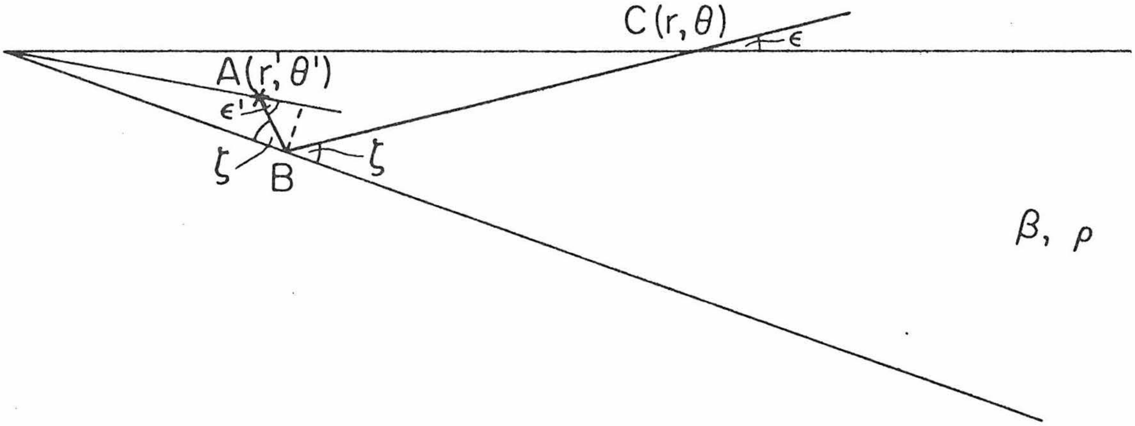

Figure 1.2 Diagram showing the geometric path of a particular ray reflecting off the lower boundary following path ABC.

$$t_0 = (\overline{AB}+\overline{BC})/\beta \tag{1.16}$$

Following the usual first-motion technique, one approximates

$$\frac{d\gamma}{dt} \cong \frac{i(t-t_0)^{-\frac{1}{2}}}{\left(2\left|\frac{\partial^2 t}{\partial\gamma^2}\right|\right)^{\frac{1}{2}}} \tag{1.17}$$

which can be written

$$\frac{d\gamma}{dt} = \frac{i\sqrt{\beta}\left[\left(\frac{r'}{\beta}\right)^2-\gamma^2\right]^{\frac{1}{4}}\left[\left(\frac{r}{\beta}\right)^2-\gamma^2\right]^{\frac{1}{4}}}{\left[2(t-t_0)\ (\overline{AB}+\overline{BC})\right]^{\frac{1}{2}}} \tag{1.18}$$

and evaluating Wn from (1.11) we obtain

$$W_n \propto (t^2-\ t_0{}^2)^{-\frac{1}{2}}\ H(t-t_0) \tag{1.19}$$

which is the behavior of the well known line source solution, see Gilbert and Knopoff (1961).

Thus, we obtain a solution consisting of generalized rays similar to the flat case except that the number of rays is finite, limited by conditions on $N_1$ and $N_2$, see appendix for details. There are also two remainder terms given in expression (1.10) that correspond to diffracted waves which do not have saddle points and are depleted in the shorter periods as discussed by Hudson (1963). When the dip is small the number of contributing rays approaches that normally used in the flat case. However, when the dip is large the number of rays allowed is relatively small and the remainder terms are proportionately larger.

*Method of equivalent models.* If we drop the term $(2\mathcal{R}n)$ in formula (1.11), we can find an equivalent model for each generalized ray. For example, suppose we examine the ray with its geometric path as shown in Figure 1.3. It is easy to show that the path in the layer is equivalent to the ray path with $B_0B_4'$ in a whole space model. Furthermore, it is convenient to choose the coordinate system (x, y, z) and to use the ray parameter, p, defined by

$$t(p) = pd + \left(\frac{1}{\beta^2} - p^2\right)^{\frac{1}{2}} h = \text{pure real} \tag{1.20}$$

At the geometric arriving time, $t_0$, p becomes $\sin(\theta)/\beta$. For a p along the de Hoop contour we assign a complex angle to it such that $p = \frac{\sin(a+bi)}{\beta}$ and the local ray parameters are defined as:

$$p_m = \frac{\sin\left[a+(m-1)\alpha+bi\right]}{\beta} \tag{1.21}$$

Thus, the SH-displacement of the n-th generalized ray becomes

$$W_n = \operatorname{Im}\left\{\frac{2\mathcal{R}\, dp/dt}{\left(\frac{1}{\beta^2} - p^2\right)^{\frac{1}{2}}}\right\}_{p \text{ along } \Psi_n} \tag{1.22}$$

where $\mathcal{R}$ is the product of all the reflection coefficients in terms of local ray parameters $P_m$'s and $\Psi_n$ is the appropriate de-Hoop contour for each ray in its equivalent model.

Following another point of view we can break the parameters d and h into smaller segments as shown in Figure 1.4. This gives

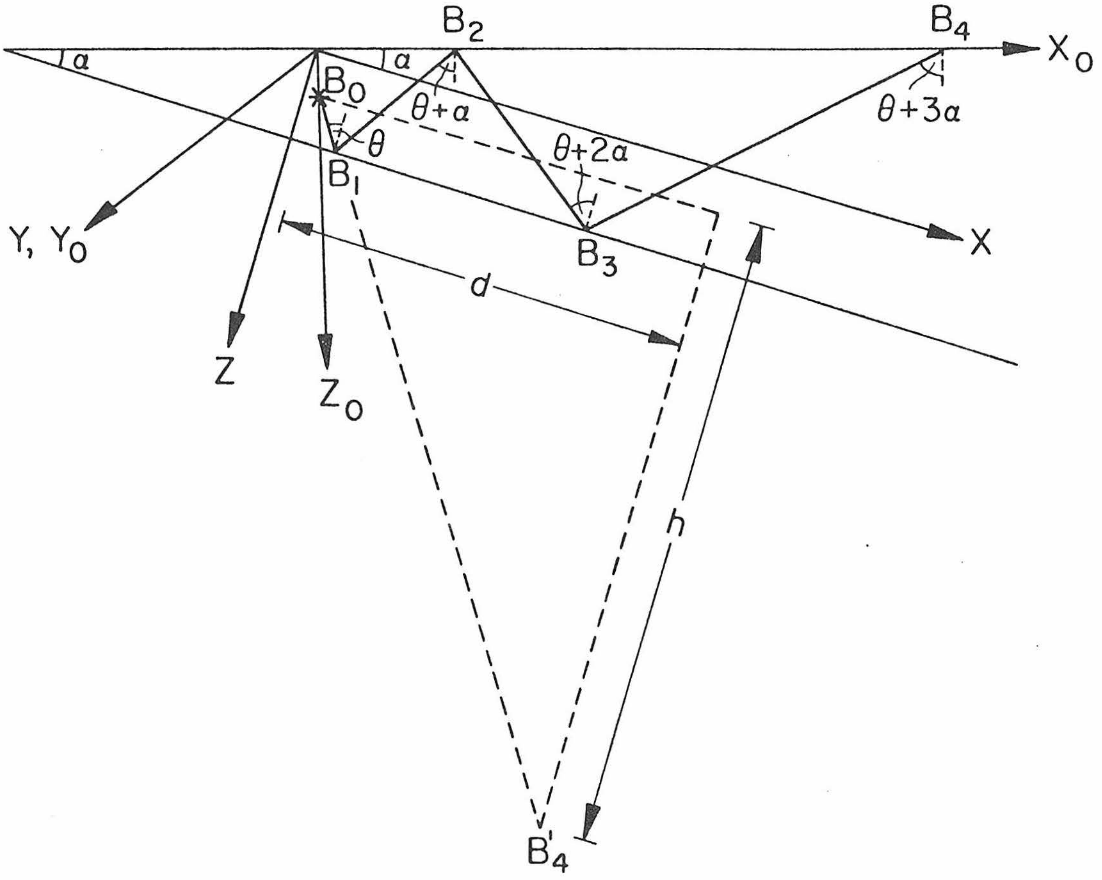

Figure 1.3 Diagram showing an equivalent model of a ray where the length of the line segment between points $B_0$ and $B_4'$ is taken to be the sum of the segments $B_0B_1$, $B_1B_2$, $B_2B_3$, and $B_3B_4$.

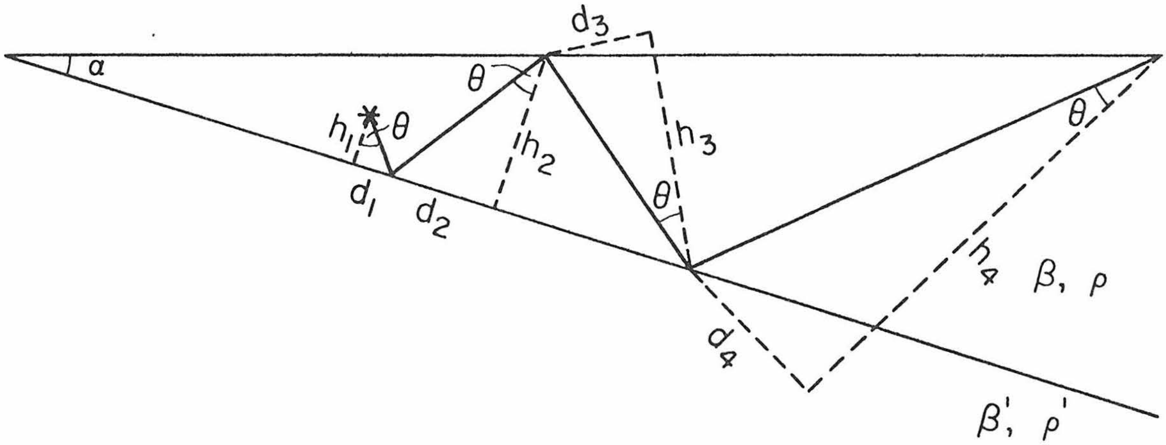

Figure 1.4 Diagram showing one kind of parameterization for a ray.

$$d = d_1 + d_2 + d_3 + d_4$$

and

$$h = h_1 + h_2 + h_3 + h_4 \qquad (1.23)$$

Now we can write the de-Hoop contour (1.20) in the following way:

$$\sum_{m=1}^{4} \left[ pd_m + (1/\beta^2 - p^2)^{\frac{1}{2}} h_m \right] = \text{pure real} \qquad (1.24)$$

We note that under an arbitrary rotation of local frames, which changes the real parts of the complex angles, the quantity $t_m = d_m \sin(a_m + b_m i) + h_m \cos(a_m + b_m i)$ is invariant, where $d_m$ and $h_m$ are defined as the horizontal and vertical projections of the segment of the geometric ray path in a frame, see Figure 1.5. Note that:

$$d \sin(a) + h \cos(a) = d' \sin(a') + h' \cos(a') \qquad (1.25)$$

$$d \cos(a) - h \sin(a) = d' \cos(a') - h' \sin(a') \qquad (1.26)$$

and thus,

$$d \sin(a+bi) + h \cos(a+bi) = d' \sin(a'+bi) + h' \cos(a'+bi) \qquad (1.27)$$

Therefore, we can reconstruct the contour (1.24) by redefining $d_m$ and $h_m$ in the following way shown in Figure 1.6.

$$\sum_{m=1}^{4} \left[ d_m \, p_m + \left( \frac{1}{\beta^2} - p_m{}^2 \right)^{\frac{1}{2}} h_m \right] = \text{pure real} \qquad (1.28)$$

Where $p_m$ is the local ray parameters defined in (1.21). The SH-displacement of the n-th generalized ray becomes:

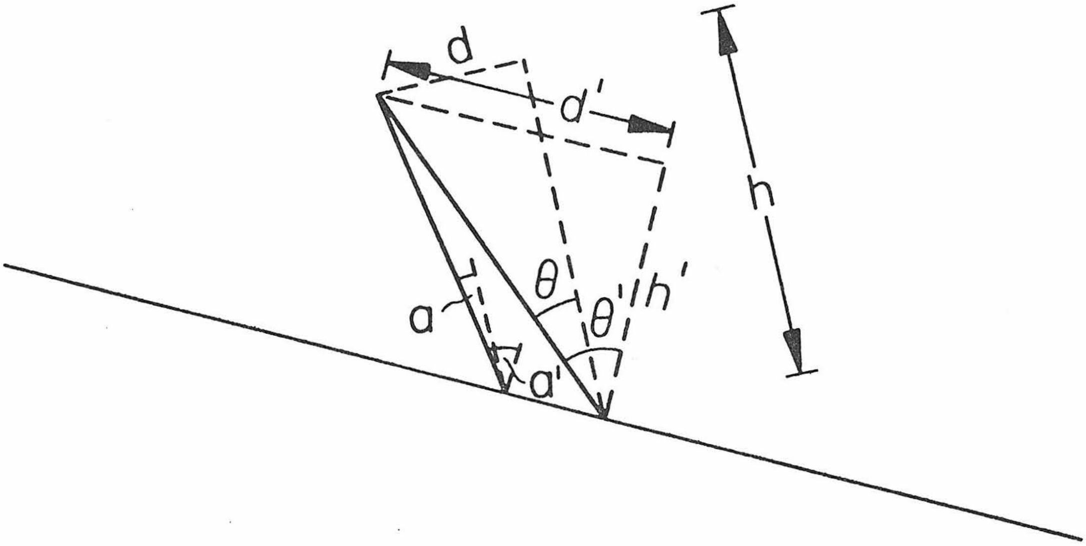

Figure 1.5 Diagram illustrates formulas (1.25) and (1.26).

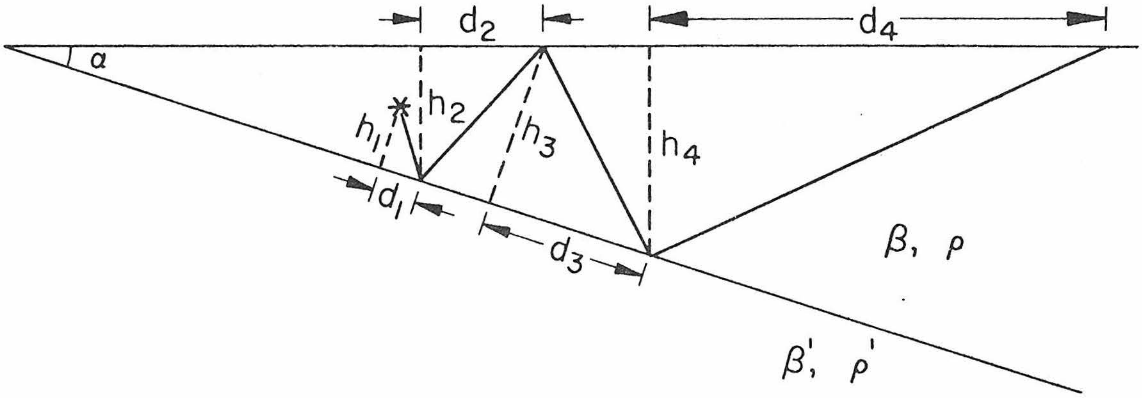

Figure 1.6  Diagram showing another kind of parameterization for a ray.

$$W_n = \mathrm{Im} \left\{ \frac{2\,\mathcal{R}\,\frac{dp_1}{dt}}{\left[(1/\beta)^2 - p_1^2\right]^{\frac{1}{2}}} \right\}_{p_1 \text{ along } \Psi_n} \tag{1.29}$$

where $\Psi_n$ is the de-Hoop contour (i.e., equation (1.28)), of the n-th generalized ray.

When the source is in the half-space, we can similarly build up the de-Hoop contour as shown in Figure 1.7.

$$\sum_{m=1}^{4} \left[ d_m\, p_m + \left(\frac{1}{\beta^2} - p_m^2\right)^{\frac{1}{2}} h_m \right] = \text{pure real}, \tag{1.30}$$

$p_m$'s are related to each other in the following way

$$\begin{aligned} p_1 &= \sin(a'+b'i)/\beta' = \sin(a+bi)/\beta \\ p_m &= \sin\left[a+(m-1)\alpha+bi\right]/\beta \quad \text{for } m=2,\ 3,\ 4 \end{aligned} \tag{1.31}$$

The SH-displacement of the (n-th) generalized ray is:

$$W_n = \mathrm{Im} \left\{ \frac{2\,\mathcal{T}\,\mathcal{R}\,\frac{dp_1}{dt}}{\left[(1/\beta)^2 - p_1^2\right]^{\frac{1}{2}}} \right\}_{p_1 \text{ along } \Psi_n}$$

where $\mathcal{T}$ is the transmission coefficient in terms of local ray parameters.

It should be noted that when we relax the rigid bottom allowing an elastic boundary, we replaced $\mathcal{R}_n$ by the product of elastic reflection-transmission coefficients in terms of the complex local ray

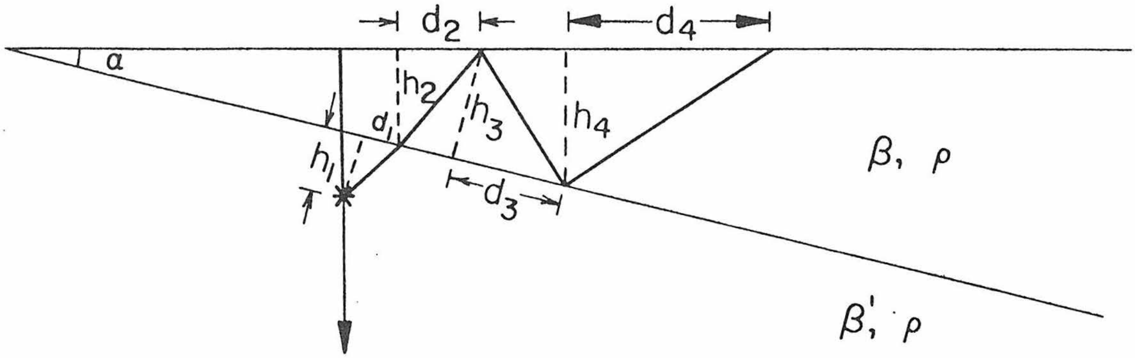

Figure 1.7 Diagram showing the parameterization of a ray with the source in the halfspace.

parameters. This approximation is essentially extended from the geometric ray theory in general structures. This enables us to evaluate nongeometric arrivals which play important roles around geometric times of multiples with critical reflections. Since this approximation lacks a rigorous theoretical basis, we need some independent checks. A comparison of results against a finite element code has been done and found to be generally accurate.

## RESULTS

In this section we present some numerical results of SH wave propagation in a layer over a halfspace. The model is given in Figure 1.8 where we have attempted to minimize diffraction effects by removing the wedge tip. We assumed a simple saw-tooth time function with a three second duration. The results are displayed in Figures 1.9 through 1.12, in which the columns on the left and middle contain individual contributions of generalized rays 1 through 4 with the summation given on the right. The higher order multiples were not included here since they are small and arrive somewhat later. All the traces on each figure are on the same amplitude scale to properly show the ray contributions.

In Figure 1.9, we fixed the source and receiver at x = 20 km and changed the dipping angle from $0^o$ to $10^o$ where the layer thickens toward the receiver, shooting down-dip. The motion behaves as if the source was actually in the layer for the larger dip angles. This effect is achieved by the simple fact that each time a ray

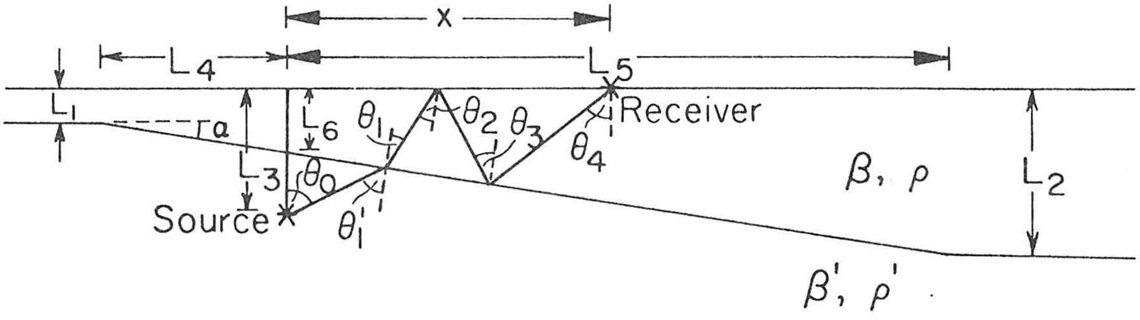

Figure 1.8 Diagram showing the labeling of model parameters.

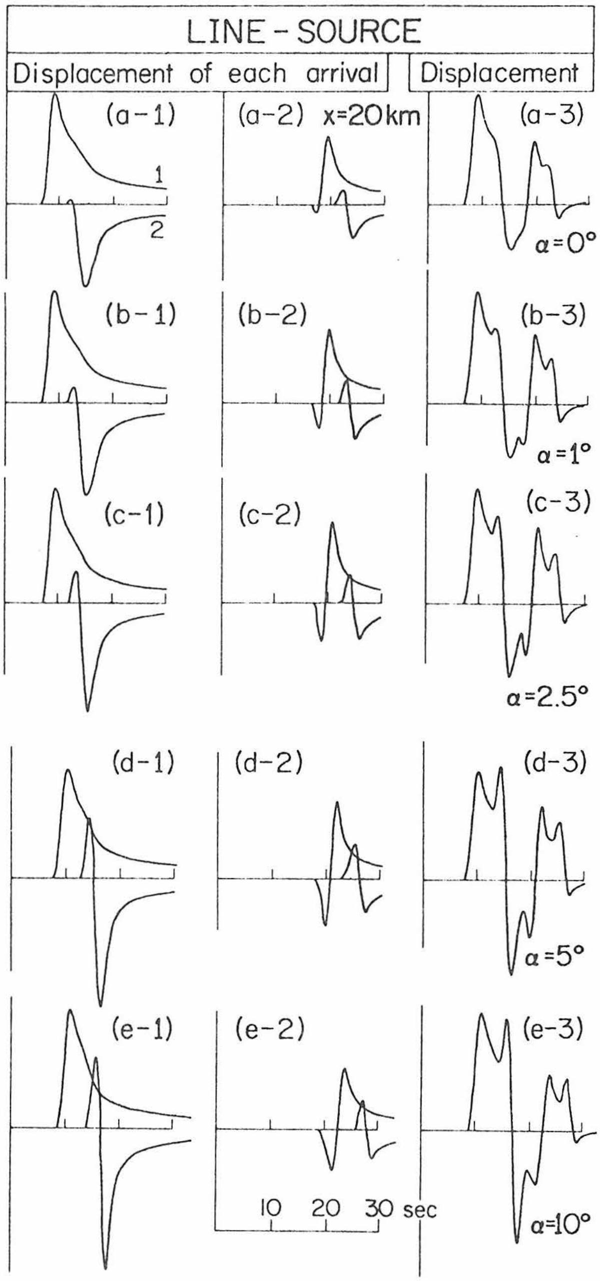

Figure 1.9 Theoretical displacements for the down-dip case with $\alpha = 0^o$ (a-3), $\alpha = 1^o$ (b-3), $\alpha = 2.5^o$ (c-3), etc. Individual ray contributions are labeled 1, 2, 3, and 4 indicating the direct, (1), followed by the one multiple, (2), etc. Column (a-1) contains rays (1) and (2) and column (a-2) contains rays (3) and (4). The summation of these four rays is given in (a-3) and similarly for the other dip angles. The common model parameters are: $L_3 = 6$ km, $L_4 = 10$ km, $L_5 = 50$ km, $L_6 = 4$ km, $x = 20$ km, $\beta = 1.6$ km/sec, $\beta' = 4.8$ km/sec, $\rho = 2.6$ gm/cm$^3$, $\rho' = 2.7$ gm/cm$^3$. The other parameters for the individual cases are: $L_1 = 4$, 3.825, 3.563, 3.125, 2.242 km and $L_2 = 4$, 4.873, 6.183, 8.376, 12.789 km for a, b, c, d, and e respectively.

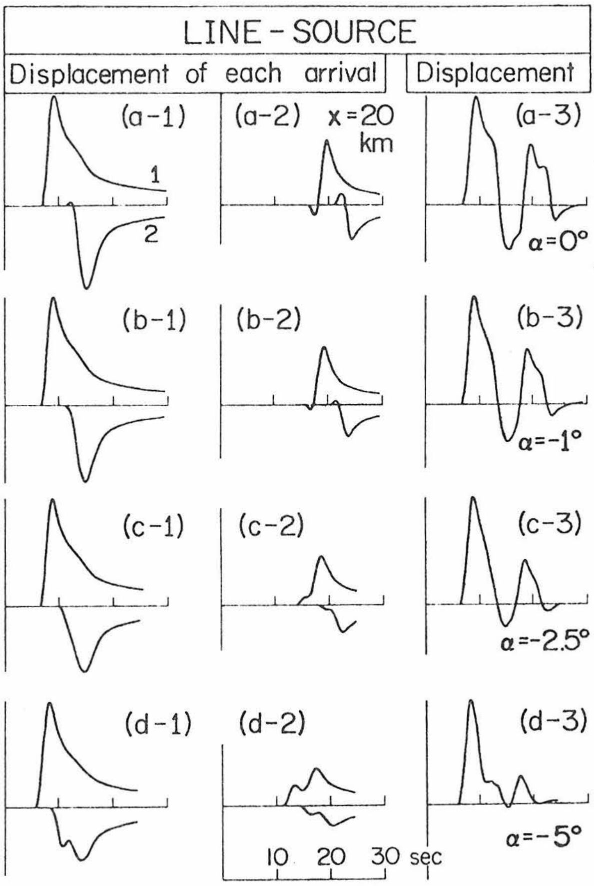

Figure 1.10 Theoretical displacements for the up-dip case with $\alpha = 0^{\circ}, -1^{\circ}, -2.5^{\circ}, -5^{\circ}$ respectively. The common model parameters are: $L_3 = 6$ km, $L_4 = 10$ km, $L_5 = 23$ km, $L_6 = 4$ km, $x = 20$ km, $\beta = 1.6$ km/sec, $\beta' = 4.8$ km/sec, $\rho = 2.6$ gm/cm$^3$, $\rho' = 2.7$ gm/cm$^3$. The other parameters for the individual cases are: $L_1 = 4$, 4.175, 4.437, 4.875 km, $L_2 = 4$, 3.599, 2.996, 1.989 km, for a, b, c, and d respectively.

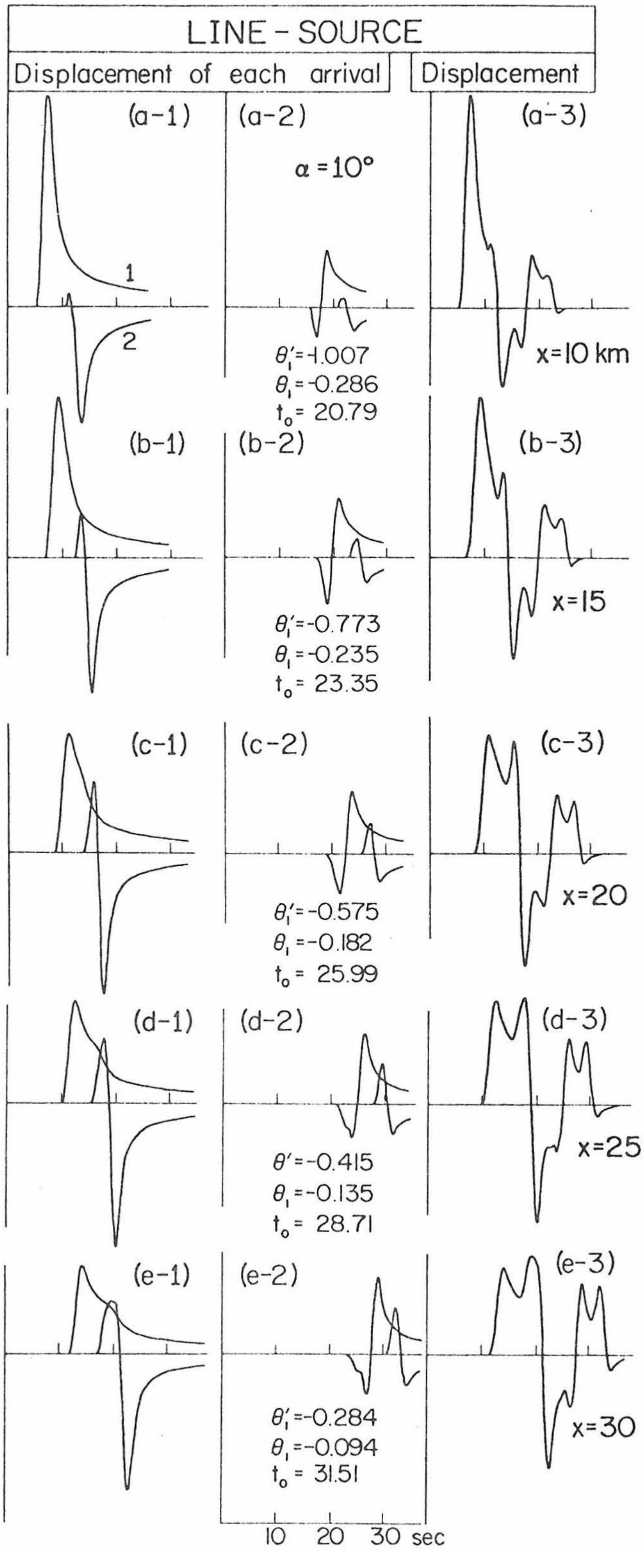

Figure 1.11 The common model parameters are $L_1$ = 2.242 km, $L_2$ = 12.789 km, $L_3$ = 6 km, $L_4$ = 10 km, $L_5$ = 50 km, $L_6$ = 4 km, and the other parameters for individual cases are: x = 10, 15, 20, 25, 30 km for a, b, c, d, and e respectively.

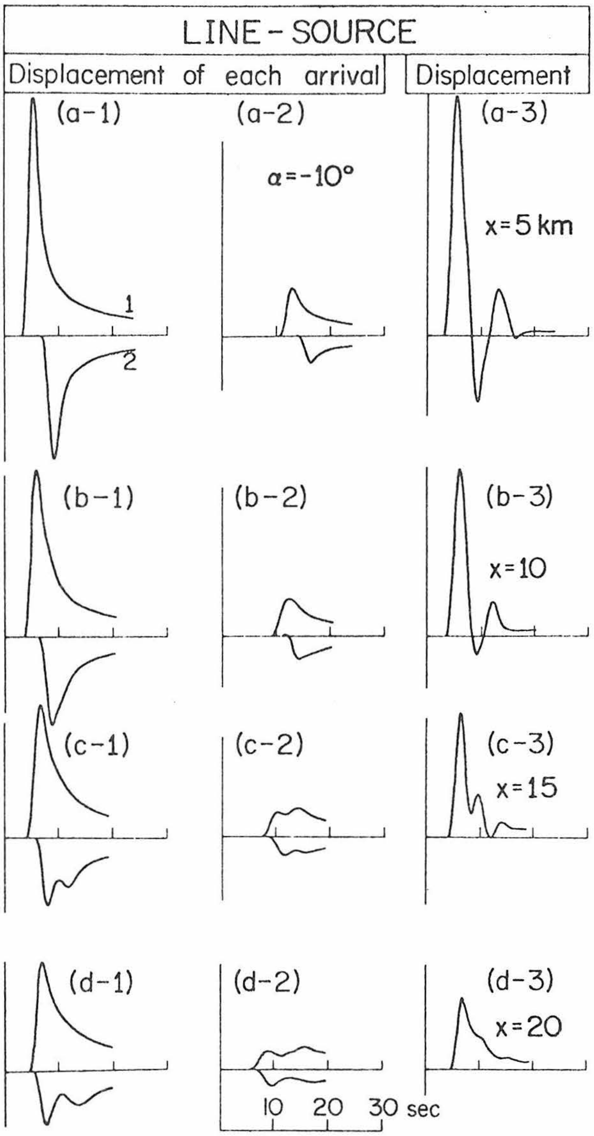

Figure 1.12 The common model parameters are $L_1$ = 5.758 km, $L_2$ = 0.484 km, $L_3$ = 6 km, $L_4$ = 10 km, $L_5$ = 22 km and the other parameters for individual cases are: x = 5, 10, 15, 20 km for a, b, c, and d respectively.

bounces in the layer its trajectory becomes flatter and can easily reach critical angle, thus producing head waves. The separation between the direct ray and multiples is increased compared to the flat case since the layer thickens towards the receiver. In this way the summation of rays produces dispersion and the development of Love waves. The opposite situation occurs when shooting up-dip, layer thinning towards the receiver. This case is displayed in Figure 1.10 where we again fix the source and receiver at x = 20 km and vary the dip angle from $0^o$ to $-5^o$. In this situation the motion behaves as if the source was somewhat deeper than it actually is when compared to the flat layer result. This effect is produced because each time a ray bounces in the layer its trajectory becomes steeper and radiates energy into the halfspace and becomes ineffectual.

One of the more interesting features produced by the dipping layer is back-scattered rays. When shooting up-dip, rays can either enter the layer beyond the receiver and, after bouncing a few times, become steeper and turn back towards the receiver. But, in general, these rays are not very large contributors because of the large loss of energy in entering the layer at these large angles of incidence.

When shooting down-dip, rays can leave the source moving away from the receiver and, after bouncing a few times in the layer, reverse their direction and return to the receiver. An example of this type of ray is given in Figure 1.11 when the dip-angle is set at $\alpha = 10^o$ and x is increased from 10 to 30 km. We have included some values of $\theta_1$ and $\theta_1'$ for ray 4 where these angles are negative. These back-scattered rays are not particularly impressive here, but they could become important in the presence of radiation pattern. A profile similar to Figure 1.11 but shooting up-dip is given in Figure 1.12 for completeness.

An interesting feature displayed by some of these rays is a tunneling effect caused by a sharp bend in the de-Hoop contour where the ray parameter remains almost real between the geometric time and the corresponding time for a source on the boundary. It is the typical behavior of a ray incident from fast region to slow region at a large angle, see Helmberger and Malone (1976). In our present case of shooting up-dip, the rays are more grazing than the corresponding ones in the down-dip case. This is the reason why the tunneling effect becomes important in the up-dip situation, for example, notice the apparent double arrival of ray 2 in Figure 1.12 (c-1) and (d-1).

## DISCUSSION

At this point, we will review the approximations made in above techniques. First, we neglected the diffracted waves associated with the wedge tip by removing the tip from the model, see Figure 1.8. Secondly, we used a high frequency approximation given by expression (1.8), and thirdly, we replaced the rigid boundary by an elastic one. Errors associated with the first and third are difficult to determine analytically, and, therefore, a series of numerical comparisons were performed to test the overall validity, as shown in Figure 3.3.

# SUMMARY

A detailed investigation of the wedge problem has confirmed earlier studies in that the motion can be constructed from rays when the diffracted wave from the wedge tip can be neglected. But instead of stopping with geometric ray theory as in the classical treatments, we have developed a scheme of mapping the de-Hoop contour by using the local complex ray parameters, thus allowing the application of generalized ray theory. This result allows us to obtain an accurate picture of the motions over a wide frequency band. Numerical motions are presented for a layer over a halfspace which display some of the important features of dipping structure as revealed by their accompanying ray expansions. The results indicate that shooting down-dip allows rapid development of Love waves by the trapping of energy in the layer. The opposite result occurs when shooting up-dip. We think there are abundant examples of this type of phenomenon observed in local earthquake records and that this technique provides a new dimension in solving these seismological problems.

# REFERENCES

Erdelyi, A., W. Magnus, F. Oberhettinger, and F. G. Tricomi (1953). Higher Transcendental Functions, Vol. 2, Bateman Manuscript Project, McGraw-Hill, New York.

Gilbert, F., and L. Knopoff (1961). The directivity problem for a buried line source, Geophysics, Vol. XXVI, No. 5, 626-634.

Helmberger, D. V., and S. D. Malone (1975). Modeling local earthquakes as shear dislocations in a layered halfspace, J. Geophys. Res., 80, 4881-4888.

Hudson, J. A. (1963). SH waves in a wedged-shaped medium, Geophys. J. Roy. Astron. Soc., 7, 517-546.

Langston, C. A. (1977). The effect of planar dipping structure on source and receiver responses for constant ray parameter, Bull. Seismol. Soc. Am. , 67 ,1029-1050.

Oberhettinger, F. (1954). Diffraction of waves by a wedge, Commun. Pure and Appl. Math, 7, 551-563.

# APPENDIX

Some of the details in the derivation of formula (1.9) were skipped in the main context. Since we think some people might be interested in how the limitation $N_1$ and $N_2$ came about we add this appendix.

$$\frac{\sinh[\lambda(\alpha-\theta')]}{\cosh(\lambda\alpha)} = \frac{2\sinh(\lambda\pi)\sinh[\lambda(\alpha-\theta')]}{2\sinh(\lambda\pi)\cosh(\lambda\alpha)}$$

$$= \frac{\cosh[\lambda\pi+\lambda\alpha-\lambda\theta']-\cosh[\lambda\pi-\lambda\alpha+\lambda\theta']}{2\sinh(\lambda\pi)\cosh(\lambda\alpha)}$$

$$= \sum_{n=0}^{N_1} \frac{(-1)^n \cosh[\lambda\pi-\lambda\theta'-2n\alpha\lambda]}{\sinh(\lambda\pi)}$$

$$+ \frac{(-1)^{N_1+1}\cosh[\lambda\pi-\lambda\theta'-(2N_1+1)\alpha\lambda]}{2\sinh(\lambda\pi)\cosh(\lambda\alpha)}$$

$$- \sum_{n=0}^{N_2} \frac{(-1)^{n-1}\cosh[\lambda\pi+\lambda\theta'-2n\alpha\lambda]}{\sinh(\lambda\pi)}$$

$$+ \frac{(-1)^{N_2}\cosh[\lambda\pi+\lambda\theta'-(2N_2+1)\alpha\lambda]}{2\sinh(\lambda\pi)\cosh(\lambda\alpha)}$$

$$\underset{\lambda\gg 1}{\cong} \sum_{n=0}^{N_1} \frac{(-1)^n e^{[\lambda\pi-\lambda\theta'-2n\alpha\lambda]}}{e^{\lambda\pi}}$$

$$+ \frac{(-1)^{N_1+1}\cosh[\lambda\pi-\lambda\theta'-(2N_1+1)\alpha\lambda]}{2\sinh(\lambda\pi)\cosh(\lambda\alpha)}$$

$$+ \sum_{n=1}^{N_2} \frac{(-1)^n e^{[\lambda\pi+\lambda\theta'-2n\alpha\lambda]}}{e^{\lambda\pi}}$$

$$+ \frac{(-1)^{N_2+1}\cosh[\lambda\pi+\lambda\theta'-(2N_2+1)\alpha\lambda]}{2\sinh(\lambda\pi)\cosh(\lambda\alpha)}$$

Here, the two conditions:

$\pi-\theta'-2N_1\alpha > 0$ and $\pi+\theta'-2N_2\alpha > 0$

are required.

# Chapter 2

# GLORIFIED OPTICS AND WAVE PROPAGATION IN NON-PLANAR STRUCTURE

# ABSTRACT

Waves propagating in varying non-planar structure can produce many interesting phenomena, such as focusing, caustics, and triplications. A high-frequency technique based on the first-motion approximation, referred to as glorified optics, has been developed to generate synthetic seismograms for these types of problems. The technique, in its simplest form, uses the spreading rate of a beam with transmission and reflection coefficients along each possible ray path. The time behavior of each arrival is either that of the original pulse or its Hilbert transform depending on the position of caustics. The geophysically interesting structure of a soft basin over a half-space is investigated in detail by this method. Synthetic seismograms appropriate for various locations are compared with the results of finite difference and finite element methods. The technique appears rich in insight and should prove very useful in modeling problems.

# INTRODUCTION

In recent years there has been a substantial increase in the number of seismic waveform inversion studies. These efforts are characterized by matching a set of records by computing synthetic waveforms for the forward problem and matching the observations by a trial and error procedure. The fits for some of the more diligent efforts are sufficiently good to allow the application of linearized inversion techniques, see for example Burdick and Mellman (1976). Unfortunately, in many studies the matching procedure can be frustrating due to the presence of scattered waves which can be readily detected by particle motion plots. However, one does not need to do much soul searching to discover abundant causes, such as basins and ridges above the source and/or similar receiver structure. The effects of basins, for example, have been well studied by Aki and Larner (1970) and Boore et al. (1971). But, because these numerical methods are so expensive one can hardly perform a parameter search to use in waveform inversion studies especially when these waveforms contain high frequency. Furthermore, most numerical methods do little to develop ones insight with respect to the physics of the problem. Thus, we have developed a technique of generating synthetics by simply tracking rays. The method is based on first motion approximations and is, therefore, a high frequency solution but appears to compare favorably to numerical experiments even at long periods in many situations.

## THEORY

Solving rigorously the boundary value problem involving complicated geometry is not possible, so we have jumped directly to an approximate form of the solution. The approximation is based on the understanding of the connection between the physical behavior of rays and the mathematical formulation for the solution of simple structures. We will introduce our technique by first reviewing the interface problem, followed by multi-dipping layers and then generalize to smoothly varying interfaces.

Fluid interface problem. We assume a point source with time history given by f(t) with the geometry specified in Figure 2.1. Applying generalized ray theory we can write down the high frequency solution, Helmberger (1968),

$$\phi(r,z,t) = f(t) * \sqrt{\frac{2}{r}}\, \frac{1}{\pi} \frac{d}{dt} \left[ \frac{1}{\sqrt{t}} * \mathrm{Im}\left( T(p) \frac{\sqrt{p}}{\eta_1} \frac{dp}{dt} \right)_{\Gamma} \right] \tag{2.1}$$

where $\phi$ is a scalar potential

$T(p)$ = transmission coefficient

$p$ = complex ray parameter

$\Gamma$ is the de-Hoop contour

$$\eta_i = \left( \frac{1}{v_i^2} - p^2 \right)^{\frac{1}{2}}$$

This solution can be simplified further by constructing the first-motion approximation for times near the direct arrival, $t_o(p_o)$

$$\frac{dp}{dt} \cong \frac{i}{[2(t-t_o)]^{\frac{1}{2}}} \left( \frac{d^2t}{dp^2} \right)^{-\frac{1}{2}}_{t=t_o} \qquad (2.2)$$

But from the geometry given in Figure 2.1 we can show that the spreading factor, $S_f$,

$$S_f \equiv \left\{ \sqrt{\frac{p}{r}}\, \frac{1}{\eta_1} \left[ \left| \frac{d^2t}{dp^2} \right| \right]^{-\frac{1}{2}} \right\}_{t=t_o} = \left( \frac{A}{A_o} \right)^{-\frac{1}{2}} \qquad (2.3)$$

where $A_o$ is the original cross-sectional area of the beam of rays at unit distance and A is the projected area at the receiver. To show this we note that

$$\eta_1 \left[ \left| \frac{d^2t}{dp^2} \right| \right]^{\frac{1}{2}} = \eta_1 \left[ \frac{h_1}{\eta_1^3 \quad v_1^2} + \frac{h_2}{\eta_2^3 \quad v_2^2} \right]^{\frac{1}{2}}$$

$$\left\{ \eta_1 \left[ \left| \frac{d^2t}{dp^2} \right| \right]^{\frac{1}{2}} \right\}_{t=t_o} = \frac{1}{\sqrt{v_1}} \left[ R_1\, d\theta_1 + R_2\, d\theta_2 \frac{\cos\theta_1}{\cos\theta_2} \right]^{\frac{1}{2}} \frac{1}{\sqrt{d\theta_1}} \qquad (2.4)$$

and,

$$\left( \sqrt{\frac{r}{p}} \right)_{t=t_o} = \left[ \frac{R_1\, \sin\theta_1 + R_2\, \sin\theta_2}{\sin\theta_1} \right]^{\frac{1}{2}} \sqrt{v_1}$$

thus,

$$S_f = \left[ \frac{(R_1 \sin\theta_1\, d\phi + R_2 \sin\theta_2\, d\phi)(R_1\, d\theta_1 + R_2\, d\theta_2\, \cos\theta_1/\cos\theta_2)}{\sin\theta_1\, d\theta_1\, d\phi} \right]^{-\frac{1}{2}} \qquad (2.5)$$

But if we let $A = A'\cos\theta_1/\cos\theta_2$ or the projection of A' onto the original orientation we obtain

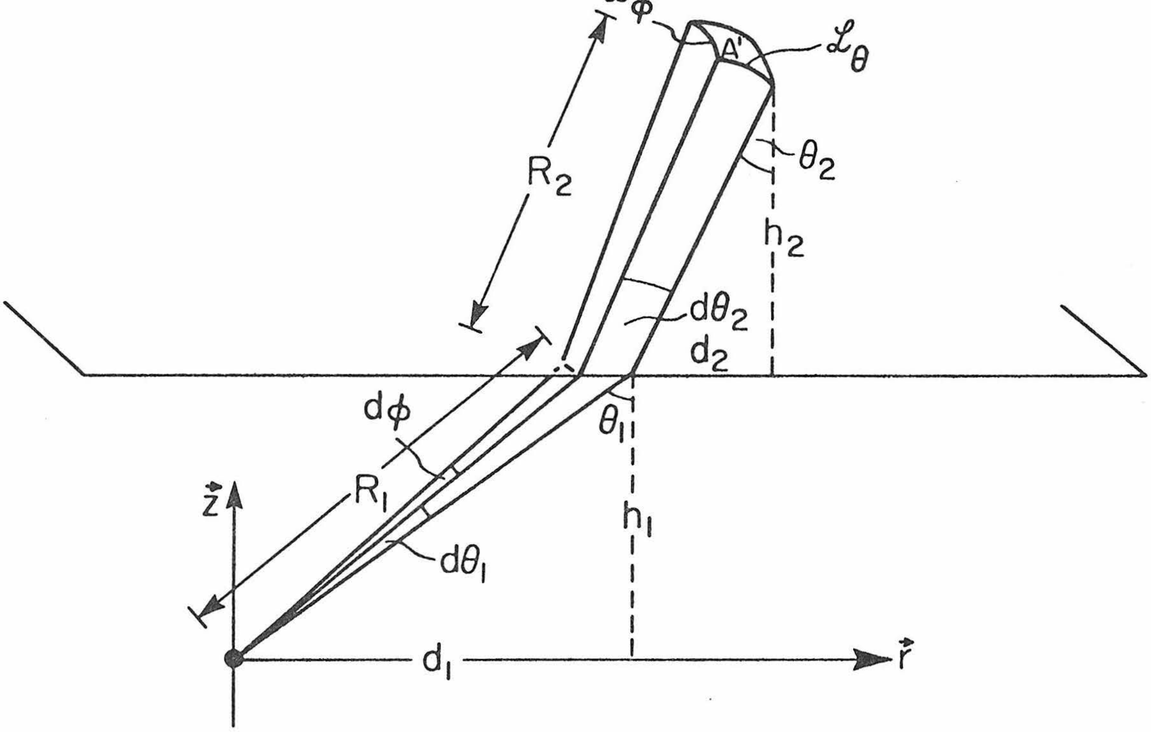

Figure 2.1 Diagram displaying the infinitesimal phenomena of geometric spreading for the simple interface problem. The area A' is the product of $\mathcal{L}_\theta$ and $\mathcal{L}_\phi$ where $\mathcal{L}_\theta = R_1 d\theta_1(\cos\theta_2/\cos\theta_1) + R_2 d\theta_2$ and $\mathcal{L}_\phi = R_1 d\phi \sin\theta_1 + R_2 d\phi \sin\theta_2$.

$$S_f = \left(\frac{A}{A_o}\right)^{-\frac{1}{2}}$$

The solution becomes

$$\phi = f(t) * \frac{1}{\pi} \frac{d}{dt}\left[\frac{1}{\sqrt{t}} * \frac{1}{\sqrt{t-t_o}}\right] \quad \mathbf{Re}[T(p_o)] \quad S_f \tag{2.6}$$

which reduced to

$$\phi = f(t-t_o) \left(\frac{A}{A_o}\right)^{-\frac{1}{2}} \quad \mathbf{Re}[T(p_o)] \tag{2.7}$$

Note that the velocity contrast across the interface changes $d\theta_1$ to $d\theta_2$ or the spreading rate in the $\theta$-direction, whereas $d\phi$ remains the same and the azimuthal spreading rate remains constant across the interface.

Dipping structure. We now consider a more general case, namely two non-parallel planar interfaces. This problem was studied in Chapter 1 assuming a line source excitation. For a point source, we require an additional complication due to spreading in the azimuthal direction. For flat structure this correction is simply $\sqrt{p/r}$ but for dipping structure we must represent it in terms of parameters in local Cartesian coordinates

$$\phi = f(t) * \frac{\sqrt{2}}{\pi} \frac{d}{dt}\left[\frac{1}{\sqrt{t}} * \operatorname{Im}\left\{ T(p) \left(\sum_{m=1}^{3} \frac{d_m}{p_m}\right)^{-\frac{1}{2}} \frac{1}{\eta_1} \frac{dp_1}{dt} \right\}_{\Gamma}\right] \tag{2.8}$$

where $p_m$ is the local ray parameter of the m-th ray segment and $d_m$ is the projection of the geometric path onto the local Cartesian coordinates, as shown in Figure 2.2. The justification for this

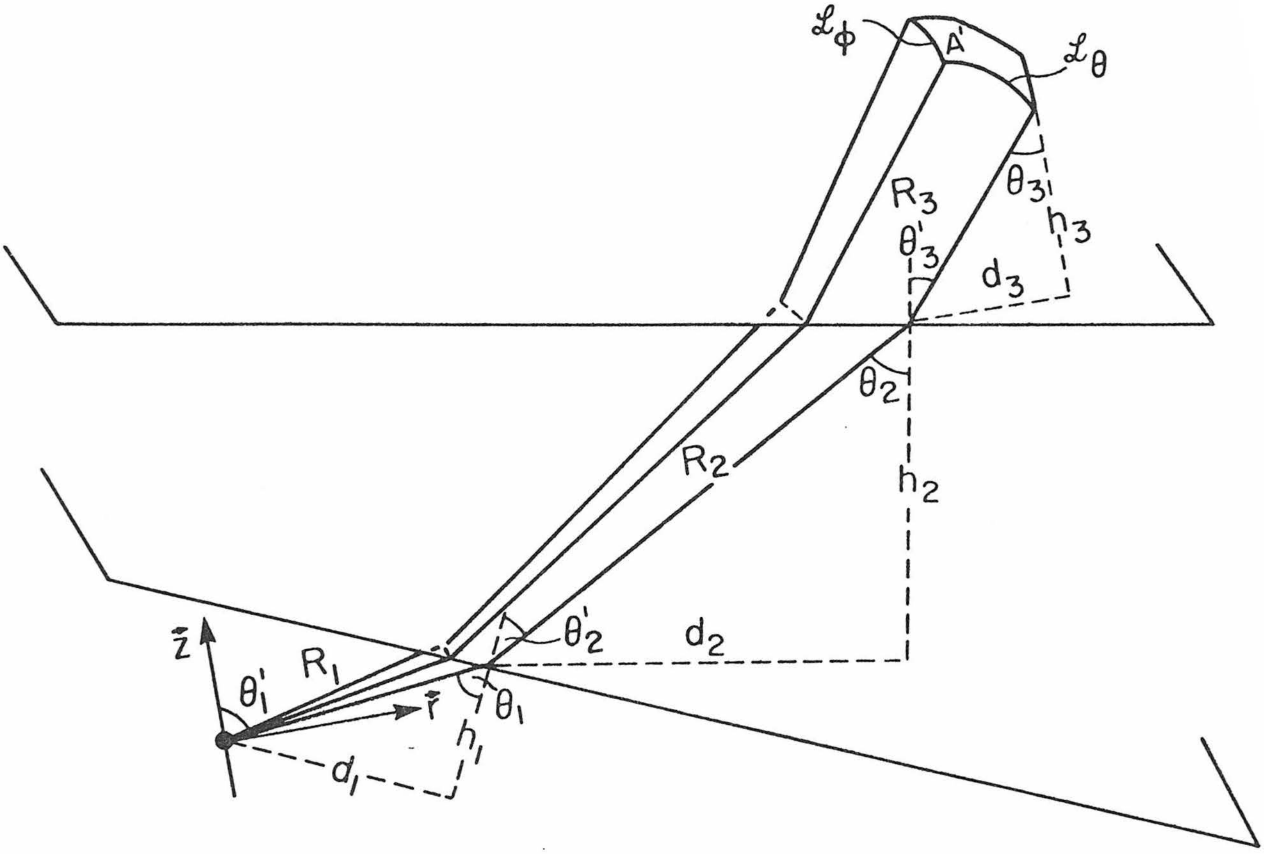

Figure 2.2 Diagram displaying the infinitesimal phenomena of geometric spreading for dipping interfaces. The area A' is the product of $\mathcal{L}_\theta$ and $\mathcal{L}_\phi$ where $\mathcal{L}_\theta = R_1 d\theta_1[(\cos\theta_2'\cos\theta_3')/(\cos\theta_1\cos\theta_2)] + R_2 d\theta_2(\cos\theta_3'/\cos\theta_2) + R_3 d\theta_3$; $\mathcal{L}_\phi = R_1\sin\theta_1 d\phi + R_2\sin\theta_2\,(\sin\theta_2'/\sin\theta_2)\,d\phi + R_3\sin\theta_3(\sin\theta_3'/\sin\theta_3)(\sin\theta_2'/\sin\theta_2)\,d\phi$ .

factor along with the details of the contour Γ are given in our earlier paper. Again, we take the first motion approximation by letting

$$\frac{dp_1}{dt} \cong \frac{i}{[2(t-t_o)]^{\frac{1}{2}}} \left( \left| \frac{d^2t}{dp_1^2} \right| \right)^{-\frac{1}{2}} \tag{2.9}$$

and after some algebra (see Appendix) we obtain

$$\eta_1 \left( \left| \frac{d^2t}{dp_1^2} \right| \right)^{\frac{1}{2}} = \frac{1}{\sqrt{v_1}} \left[ R_1 d\theta_1 + R_2 d\theta_2 \frac{\cos\theta_1}{\cos\theta_2'} + R_3 d\theta_3 \frac{\cos\theta_2}{\cos\theta_3'} \frac{\cos\theta_1}{\cos\theta_2'} \right]^{\frac{1}{2}} \frac{1}{\sqrt{d\theta_1}} \tag{2.10}$$

and, $$\left( \sum_{m=1}^{3} \frac{d_m}{p_m} \right)^{\frac{1}{2}} = \frac{\left( d_1 + d_2 \frac{\sin\theta_2'}{\sin\theta_2} + d_3 \frac{\sin\theta_3'}{\sin\theta_3} \frac{\sin\theta_2'}{\sin\theta_2} \right)^{\frac{1}{2}} \sqrt{v_1}}{(\sin\theta_1)^{\frac{1}{2}}} \tag{2.11}$$

thus, $$S_f = \left( \sum_{m=1}^{3} \frac{d_m}{p_m} \right)^{-\frac{1}{2}} \frac{1}{\eta_1} \left| \frac{d^2t}{dp_1^2} \right|^{-\frac{1}{2}} = \left( \frac{A}{A_o} \right)^{-\frac{1}{2}} \tag{2.12}$$

where $A = A' \dfrac{\cos\theta_1}{\cos\theta_2'} \dfrac{\cos\theta_2}{\cos\theta_3'}$

or the projection of A' given in Figure 2.2 back into the original orientation. The solution becomes

$$\phi = f(t-t_o) \left( \frac{A}{A_o} \right)^{-\frac{1}{2}} \mathrm{Re}[T(p_o)] \tag{2.13}$$

where we must compute the transmission coefficients with the appropriate local ray parameter ($p_m$). Calculating ($A/A_o$) analytically for a large number of ray segments is laborious but could be done. A much more practical approach and one we recommend is to simply add a small ($\delta p$) to the proper ray parameter, $p_o$ , that p required to track a ray from the source to the receiver and measure ($A'/A_o$) numerically, or more precisely

$$\lim_{\delta p \to 0} \left( \frac{A}{A_o} \right) = \lim_{\delta p \to 0} \left\{ \left( \frac{\mathcal{L}_\theta}{A_o} \right) \mathcal{L}_\phi \left[ \frac{\cos\theta_1}{\cos\theta_2'} \cdots \frac{\cos\theta_n}{\cos\theta_{n+1}'} \right] \right\} \tag{2.14}$$

where the azimuthal spreading

$$\lim_{\delta \phi \to 0} \left( \frac{\mathcal{L}_\phi}{\delta \phi} \right) = p_1 \left( \sum_m \frac{d_m}{p_m} \right) \tag{2.15}$$

can be computed analytically. The numerical procedure is required to obtain the limiting value on $\mathcal{L}_\theta$ when its behavior becomes highly complicated with the addition of curvature as we will demonstrate shortly.

Periodical semi-circular boundary. In this section we apply our technique to a simple curved boundary such that the limiting process can be performed analytically in the presence of caustics. For convenience, we will assume a plane wave source at vertical incidence to eliminate $\mathcal{L}_\phi$ contributions. The geometrical considerations displaying focusing and other complications are given in Figure 2.3. We begin as before by investigating the spreading rate for a particular ray as shown in Figure 2.4. The function description of the boundary for the assumed coordinate system is

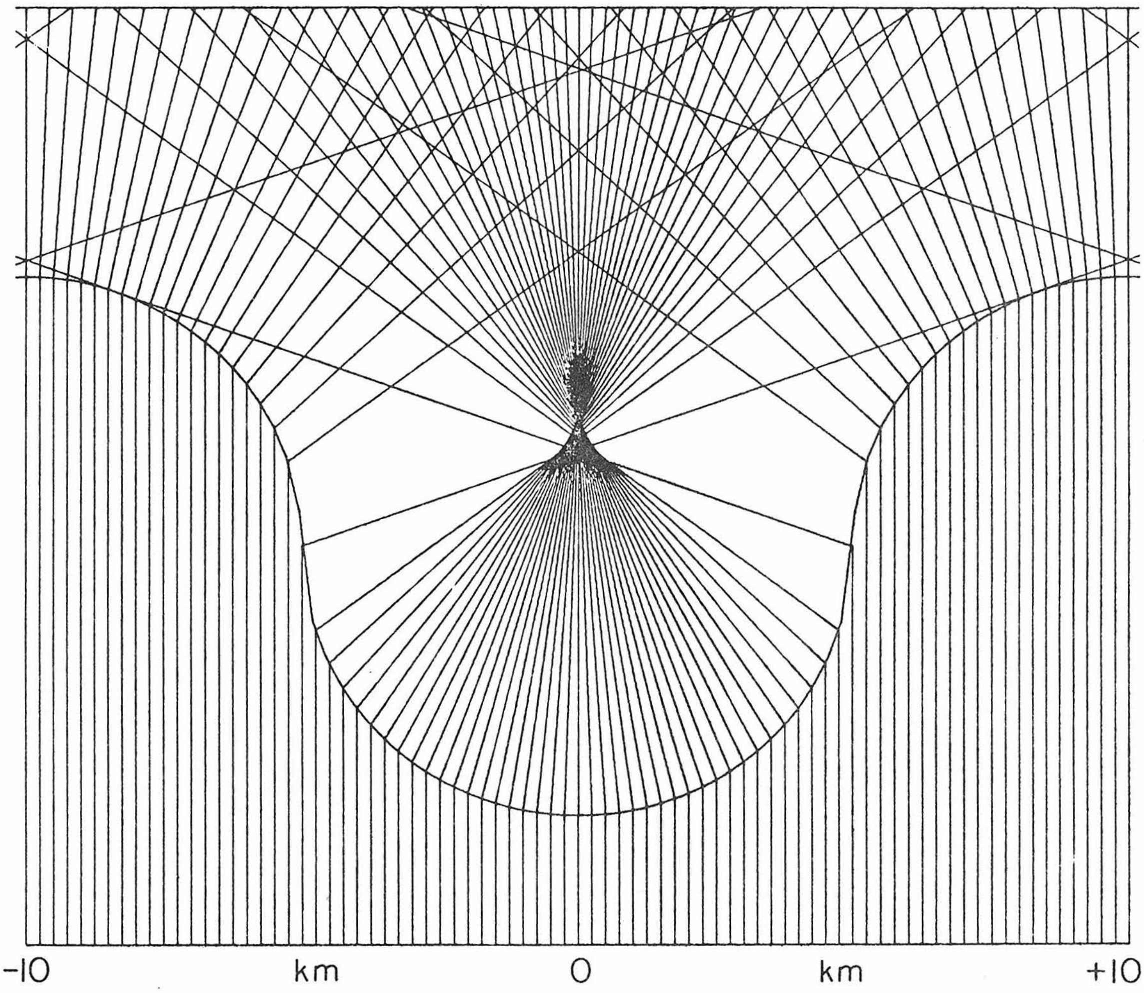

Figure 2.3 Diagram showing the bending of geometric ray paths caused by a periodic semi-circular interface.

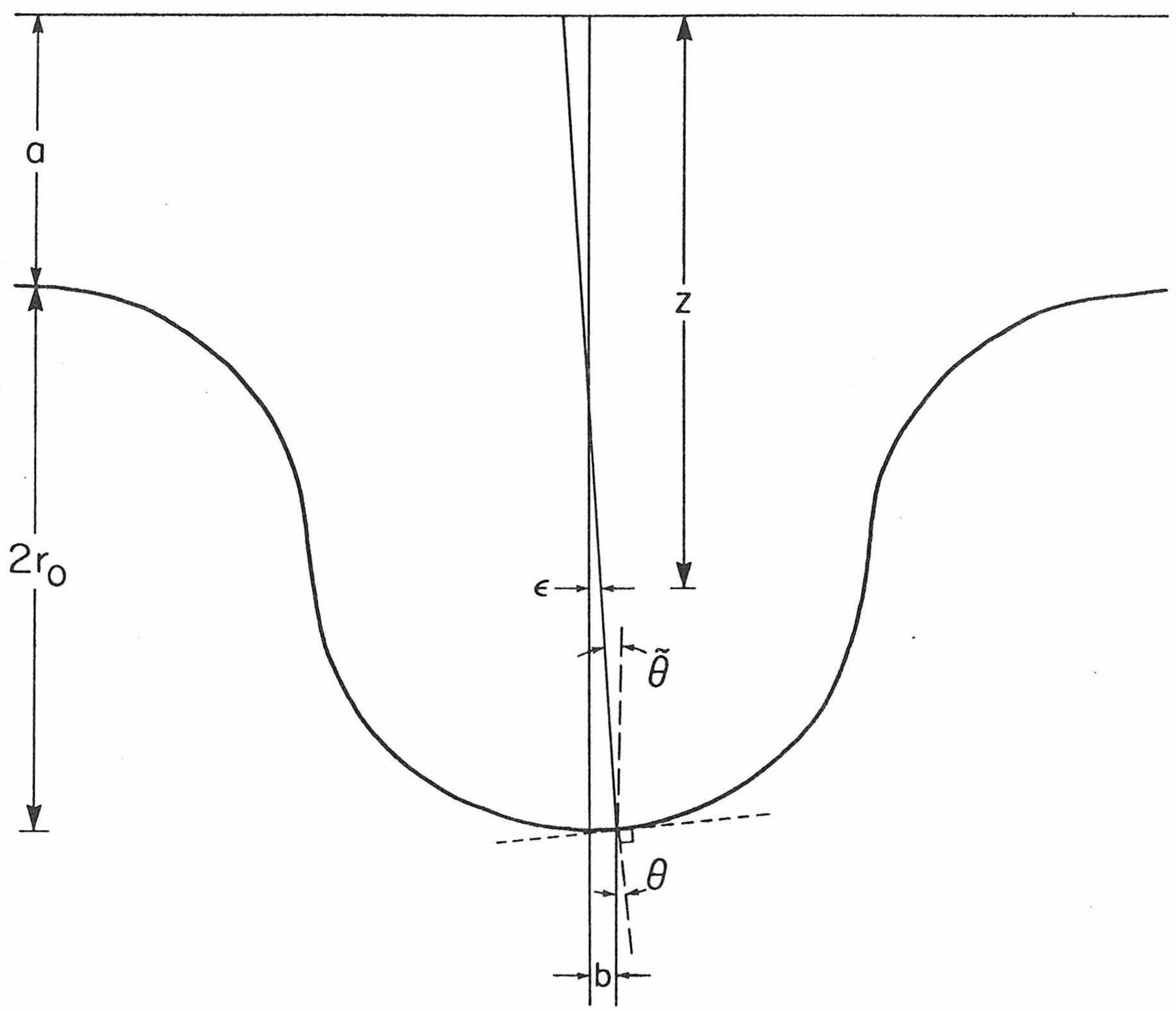

Figure 2.4 Diagram displaying the infinitesimal phenomena of geometric spreading for a curved boundary. The parameters are a = 5 km, $r_o$ = 5 km, the upper velocity ($v_1$) is 1 km/sec and the lower velocity ($v_2$) is 3 km/sec, and the density is assumed constant.

$$\left[z-(a+r_o)\right]^2+x^2 = r_o^2 \quad , \qquad \text{for } -r_o \leq x \leq r \tag{2.16}$$

The angle between the local normal and the vertical is

$$\theta(x) = \tan^{-1}\left[x/(r_o^2-x^2)^{\frac{1}{2}}\right] \tag{2.17}$$

and, further, let

$$\tilde{\theta}(x) = \theta-\sin^{-1}(v_1\sin\theta/v_2)$$

where $v_1$ and $v_2$ are the velocities in the upper and lower media respectively. The spreading element, $\varepsilon$, is

$$\varepsilon = b-\left[(a+r_o)+(r_o^2-b^2)^{\frac{1}{2}}-z\right]\tan\tilde{\theta} \tag{2.18}$$

from the geometry given in Figure 2.4. Next, we perform the limiting process

$$\lim_{b\to 0}\left(\frac{\varepsilon}{b}\right) = 1-[a+2r_o-z]\left\{\lim_{b\to 0}\left[\frac{d}{db}\tan\tilde{\theta}\right]\right\} \tag{2.19}$$

$$\frac{d}{db}\tan\tilde{\theta} = \frac{1}{\cos^2\tilde{\theta}}\left[1-\frac{\frac{v_1}{v_2}\cos\theta}{\left(1-\frac{v_1^2\sin^2\theta}{v_2^2}\right)^{\frac{1}{2}}}\right](r_o^2-b^2)^{-\frac{1}{2}} \tag{2.20}$$

$$S_f = \lim_{b\to 0}\left\{\left(\frac{A}{A_o}\right)^{-\frac{1}{2}}\right\} = \left[1-(a+2r_o-z)\left(1-\frac{v_1}{v_2}\right)\frac{1}{r_o}\right]^{-\frac{1}{2}} \tag{2.21}$$

Note that A can be negative and there is a singular point along this geometric ray path with z defined by

$$z = a+2r_o-r_o/(1-v_1/v_2) \tag{2.22}$$

which is dramatically displayed in Figure 2.3. Our solution fails at this point but could be salvaged by using the third order saddle-point approximation. For

$$z < a+2r_o-r_o/(1-v_1/v_2)$$

we cross the caustic and the $90^o$ phase shift occurs, see Hill (1974) for a discussion of such effects.

In cases involving multiple reflections the generalized coefficient containing the product of all interactions expressed simply as T(p) can become complex, so that in general for $(A/A_o) > 0$ ,

$$\begin{aligned}\phi = {} & f(t-t_o)\mathrm{Re}\left[T(p_o)\right] |S_f| \\ & + f^*(t-t_o)\,\mathrm{Im}\left[T(p_o)\right] |S_f|\end{aligned} \tag{2.23}$$

Similarly, for $(A/A_o) < 0$, the response becomes

$$\begin{aligned}\phi = {} & f^*(t-t_o)\mathrm{Re}\left[T(p_o)\right] |S_f| \\ & + f(t-t_o)\,\mathrm{Im}\left[T(p_o)\right] |S_f|\end{aligned} \tag{2.24}$$

where $f^*(t-t_o)$ is the allied function of $f(t-t_o)$, that is the same amplitude spectra but with a $90^o$ phase shift.

In the next section we will generate synthetics for a soft basin over a half-space using several methods. Thus, as a preliminary comparison we compute the responses for the periodic structure at x = 0 and x = 10 km as displayed in Figure 2.5. These two ranges were chosen to further test the phase shifts discussed above. If we number the rays left to right we see that the second or middle ray is phase-shifted for x = 0 whereas the second and fourth rays are phase-shifted at x = 10 km. Glorified optics results (GO) are obtained by simply adding the rays shown in Figure 2.5 applying equations (2.23) and (2.24). The source function and its allied function are displayed at the bottom of Figure 2.6 with the synthetics given above along with the finite element results. The comparison is good considering the nature of the source. That is, glorified optics is expected to give the most accurate result for short periods, thus the drift effects occurring in the GO synthetics are caused by the large offset in the assumed source. There are, also, errors associated with using the flat-layer transmission coefficient which could be easily corrected for local curvature. However, we are primarily concerned with focusing and defocusing in this particular study since such effects appear dominant.

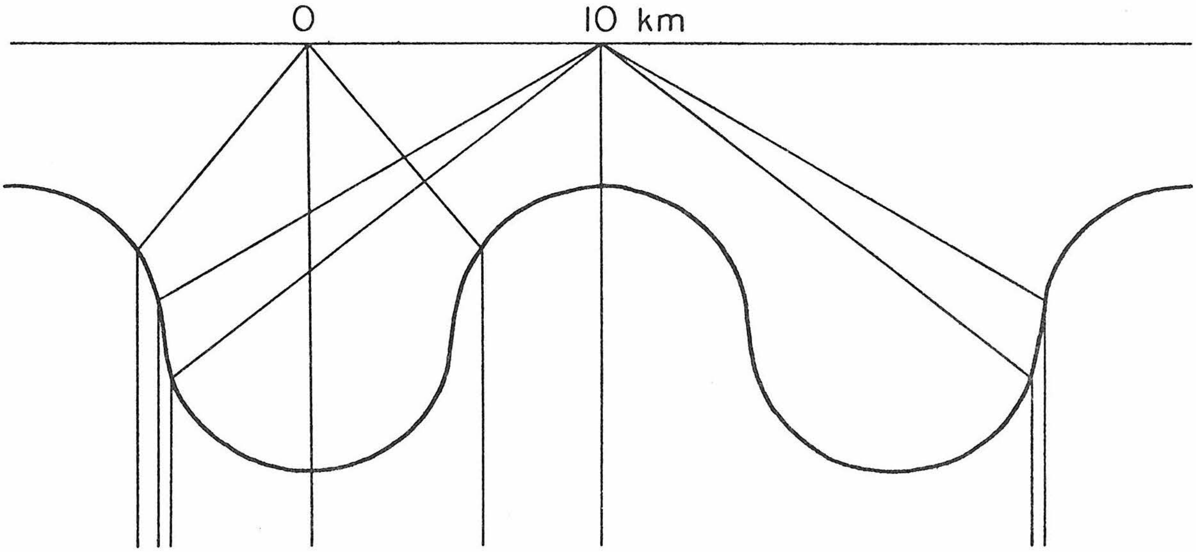

Figure 2.5 Diagram showing the paths of geometric rays arriving at x = 0 km, z = 0 km; and x = 10 km, z = 0 km.

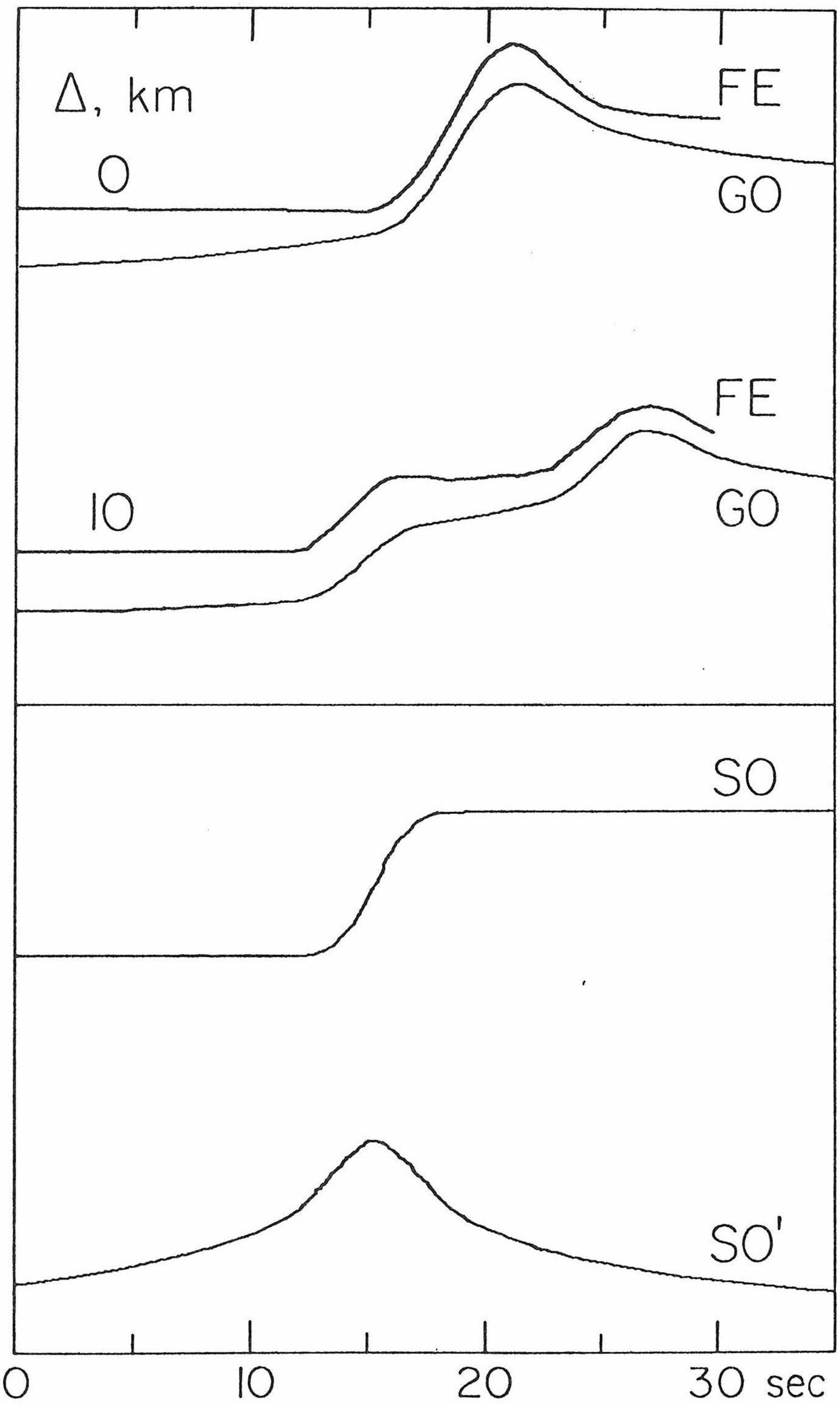

Figure 2.6 Comparison of SH displacements received at the two locations shown in Figure 2.5. The traces marked with FE are by finite element method. Those marked with GO are by glorified optics.

## RESULTS

Since our technique is a first order approximation it is prudent to test its validity against other more exact techniques such as the numerical methods discussed by Aki and Larner (1970), the finite difference method, Boore et al. (1971) or the finite element method, see Chapter 3. These numerical methods are basically long period techniques in that the grid size must be large enough to make the method affordable. On the other hand, glorified optics become increasingly accurate as the frequency is increased, thus the various methods complement each other. Boore et al. (1971) have already performed a detailed comparison between the AL method and finite difference results for basin structures. We will attempt to match Boore's results using their model parameters and source description specified below.

The curved boundary describing the bottom of the basin is

$$z(x) = -D - \frac{C}{2}\left\{1-\cos\left[2\pi\left(x-\frac{w}{2}\right)/w\right]\right\}, \qquad \text{for } -\frac{w}{2} \le x \le \frac{w}{2}$$

$$z(x) = -D \quad , \quad \text{elsewhere} \tag{2.25}$$

where $w = 50$ km, $D = 1$ km, and $C = 5$ km. A plane SH wave with source time function, $f(t)$, is impinging vertically from the half-space,

$$f(t) = \frac{\sqrt{\pi}}{2}\left(a - \frac{1}{2}\right)\exp(-a) \tag{2.26}$$

where,

$$a = 6(t-t_s)^2 \Big/ \left(T_p \cdot \frac{\sqrt{6}}{\pi}\right)$$

$$t_s = 20 \text{ sec.} \quad , \quad T_p = 18.3 \text{ sec.}$$

The density and velocity in the basin are $\rho_1 = 2\ gm/cm^3$, $\beta_1 = 0.7\ km/sec$ respectively, and $\rho_2 = 3.3\ gm/cm^3$, $\beta_2 = 3.5\ km/sec$, in the half-space.

The basin structure with the direct, and two sets of multiply reflected ray paths are displayed in Figure 2.7. The qualitative characteristics of the motion can be seen by observing the focusing of the multiples and development of caustics. For instance, the first multiples at the center of the basin focus rather strongly which will give rise to a large second arrival at this position. For longer times, rays begin to come in from the sides. Since our model is a ray method it is educational to observe the development of the motion as a function of ray summation for a couple of positions, see Figures 2.8 and 2.9 for the center position and Figures 2.10 and 2.11 for a station close to the edge of the basin. In Figure 2.8, we display the rays by the number of times they are reflected internally starting at the top; that is (1) contains the direct, (2) contains one multiple and one ray, (3) contains two multiples but three rays, etc. The synthetic contribution from (1), (2), (3), and etc. are displayed in Figure 2.9 individually with the final summation of all responses given at the bottom. Note that the rays bouncing vertically contribute very little after two reflections whereas the rays coming in from the sides are heavy contributors at large times because of the large low angle reflections. The rays that enter on one side of the basin and travel across the basin internally and return again are sometimes large but usually small depending on focusing. The observations at the edge, or off center, are more interesting in many ways due to the large

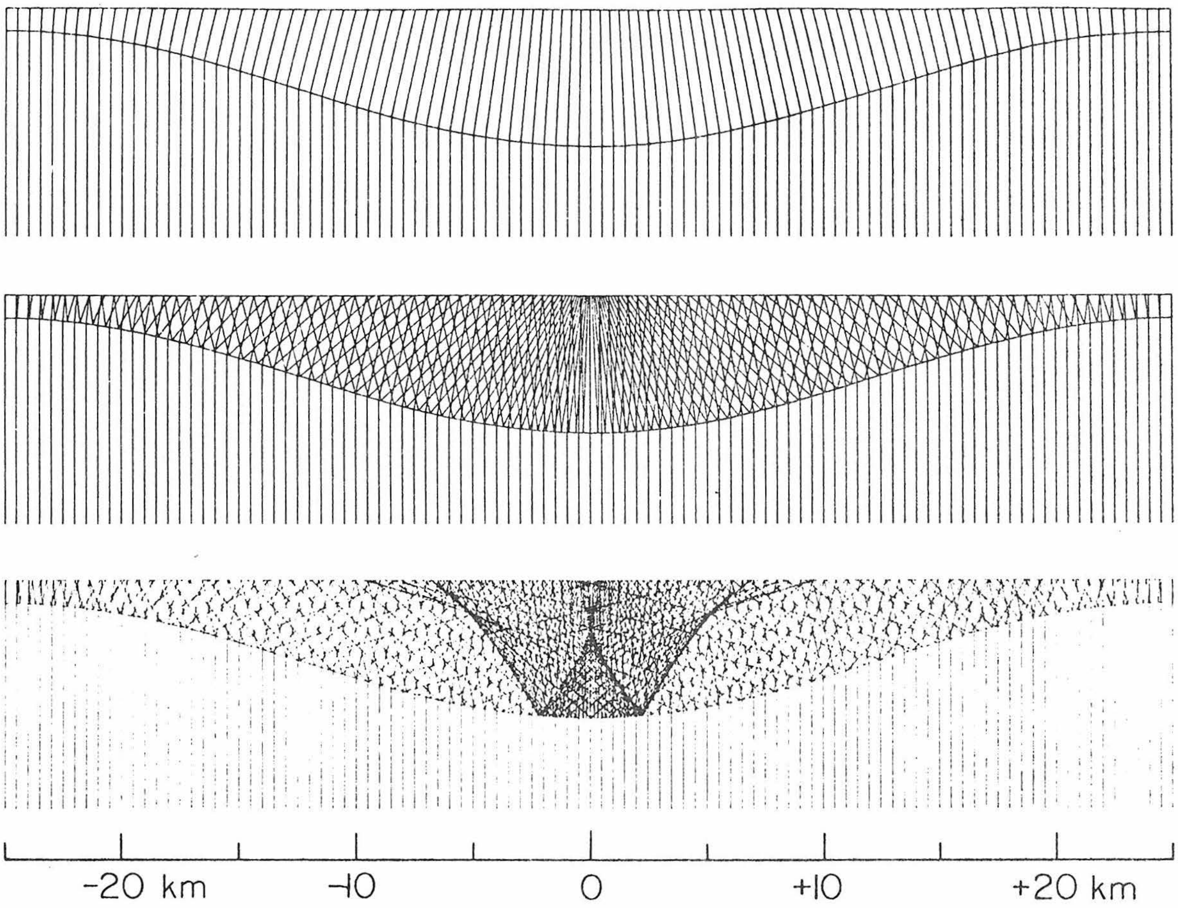

Figure 2.7a Diagram showing the paths of geometric rays; the direct rays on the top; the rays with two reflections in the middle; the rays with four reflections on the bottom.

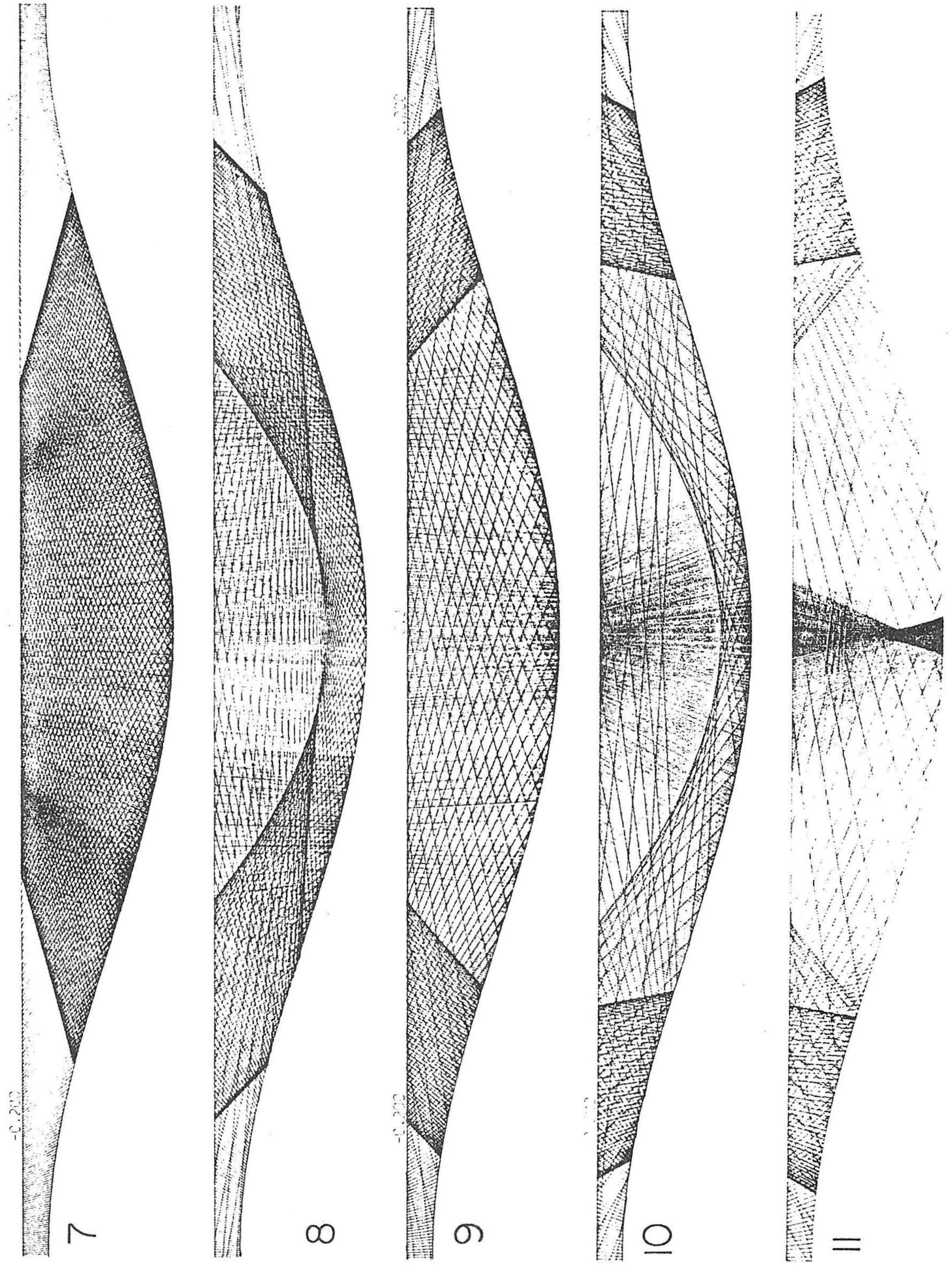

Figure 2.7b Patterns of the caustics formed by higher multiples.

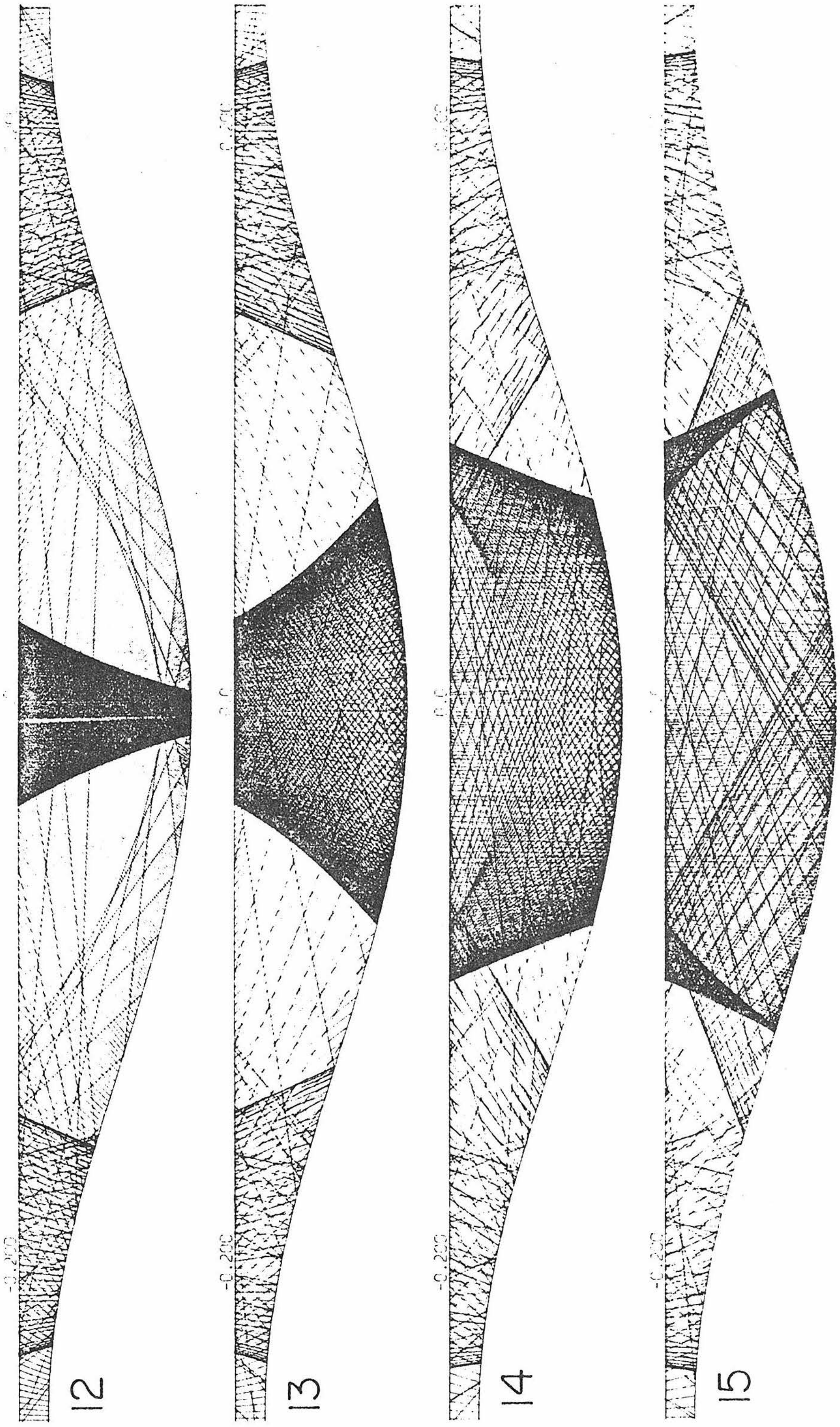

Figure 2.7c Continuation of Figure 2.7b.

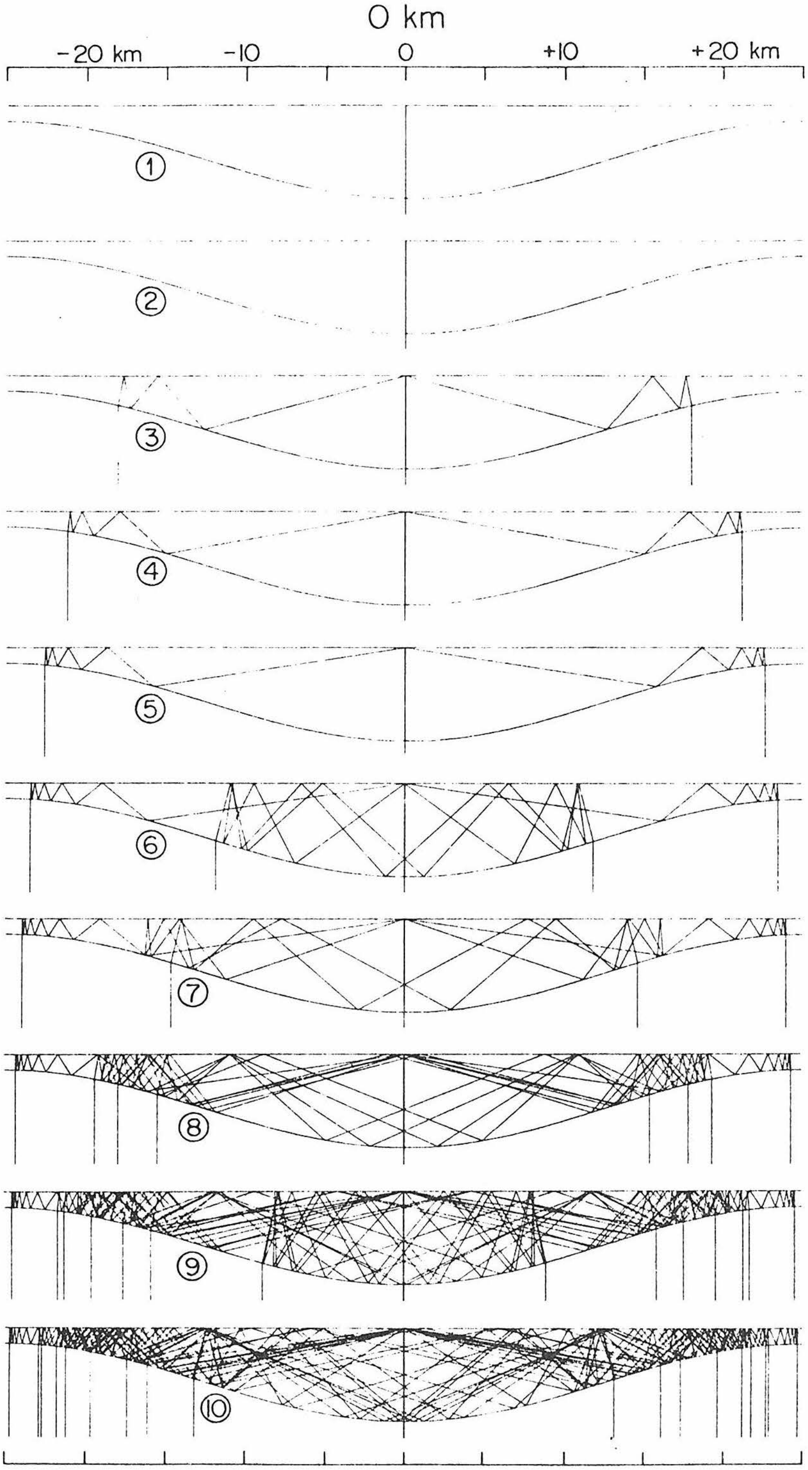

Figure 2.8 The paths of geometric rays arriving at x = 0. The top trace, (1), contains the direct ray, and (2) displays the ray with two reflections, etc.

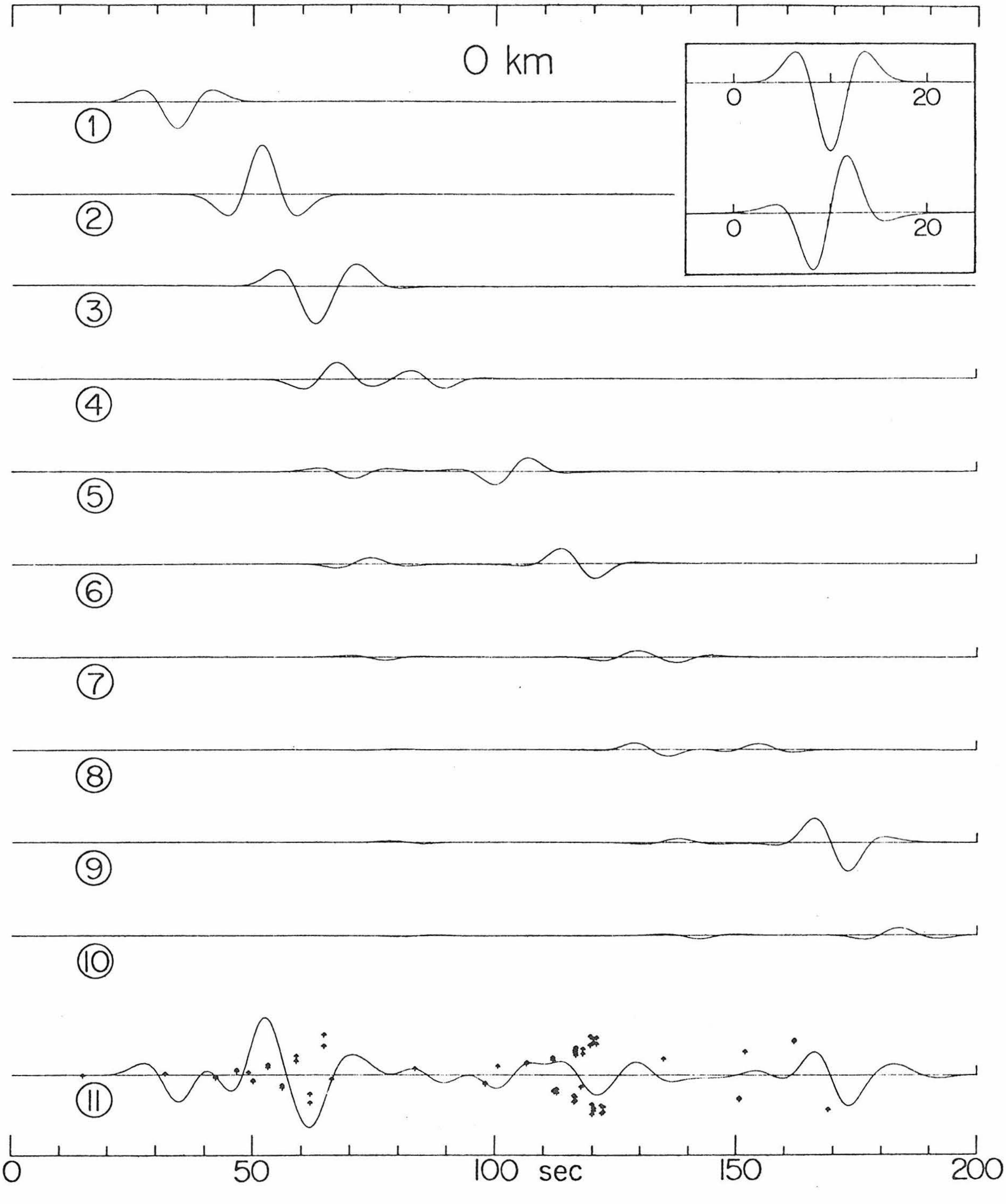

Figure 2.9 Diagram showing the contribution of each set of rays displayed in Figure 2.8 with the final summation at the bottom. Arrows indicate arrival times.

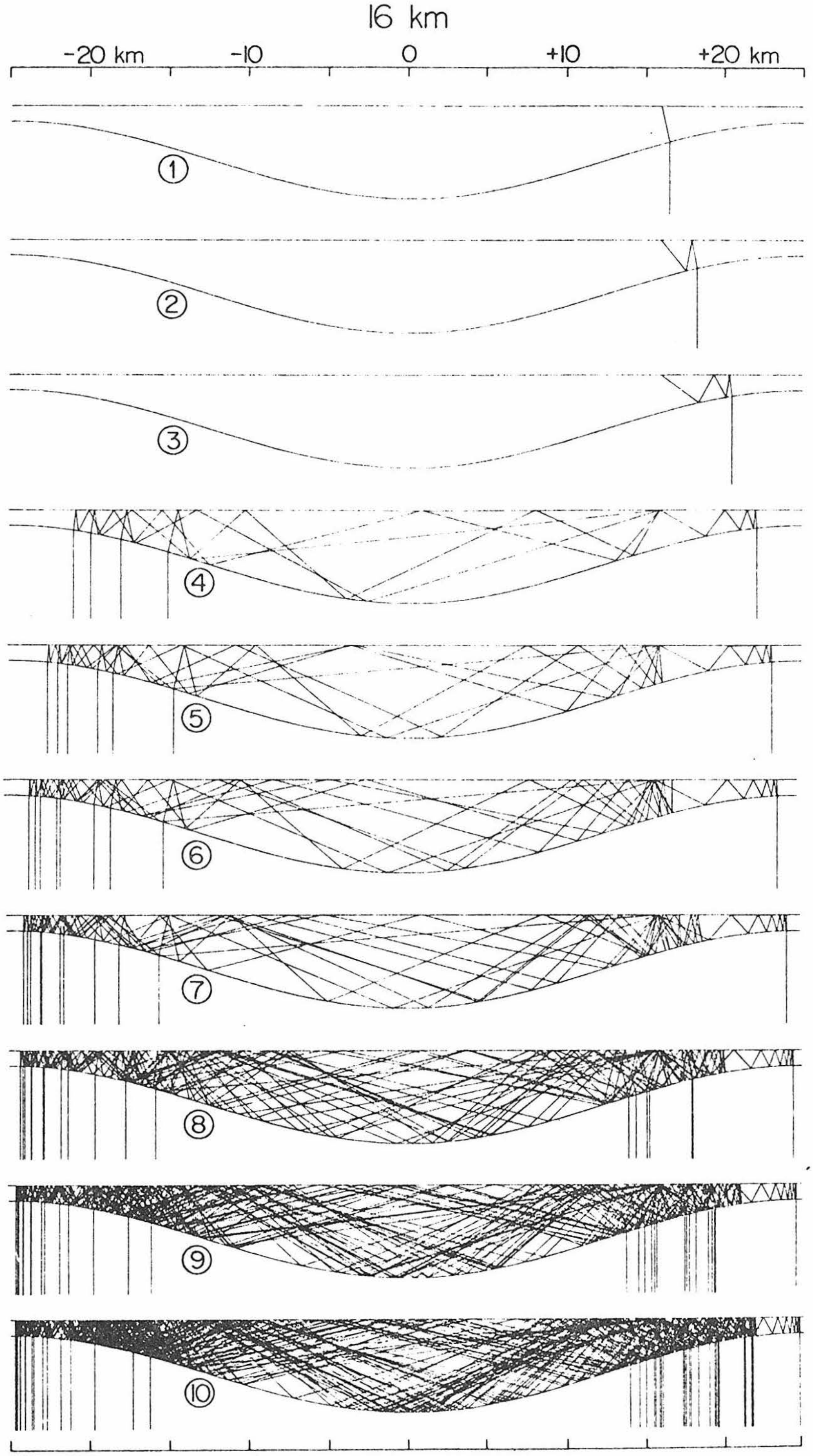

Figure 2.10 The paths of geometric rays arriving at x = 16 km. The top trace, (1), contains the direct ray, and (2) displays the ray with two reflections, etc.

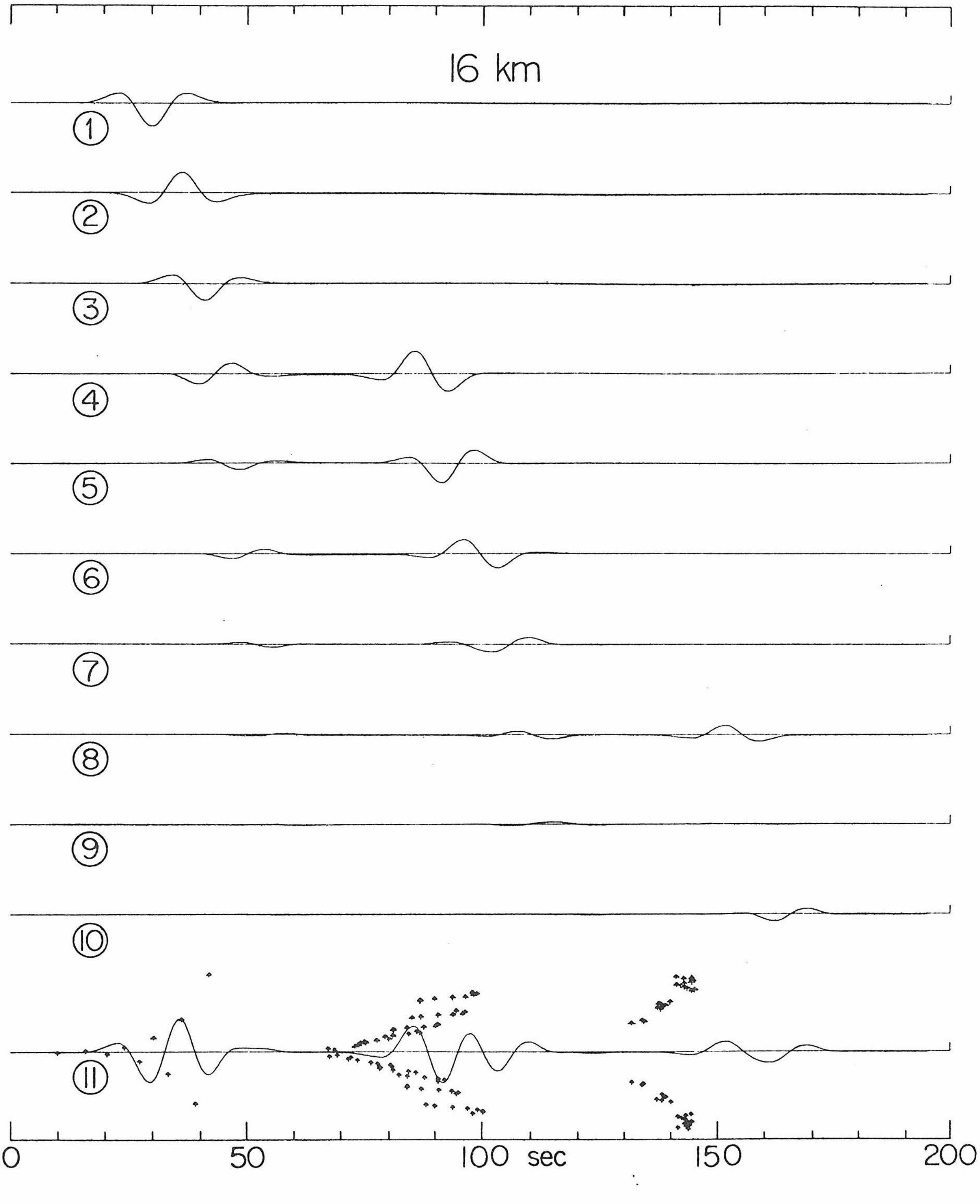

Figure 2.11 Diagram showing the contribution of each set of rays displayed in Figure 2.10 with the final summation at the bottom. Arrows indicate arrival times.

contributions that come from the opposite side of the basin at later times as is apparent from Figures 2.10 and 2.11.

The results at various ranges after summing the first 10 sets of rays are displayed in Figure 2.12 along with the comparisons with numerical methods. It is relatively expensive to compute the numerical results at large times which is the reason for the truncations, see Boore et al. (1971) and Hong and Kosloff (1978). Considering the simplicity of the glorified optics method it is rather surprising that the agreement is so good. In general, the beginning portion of each record appears very accurate which corresponds to rays traveling nearly vertical. At later times, the GO results appear less accurate which corresponds to rays traveling more nearly horizontal. This probably means that the curvature of the boundary becomes more important and higher order reflection coefficients may be necessary. Rays that travel from one wall of the basin to the other side without hitting the surface were also considered but found to be weak contributors.

The results with a shorter period time function are given in Figure 2.13, where some of the amplified arrivals are more apparent such as the first multiple at $x = 0$. It is relatively important for these large signals to perform the limiting process carefully. That is, we examine the ratio of areas for a narrow beam of area $A_o$ and test for stability by considering a series of smaller and smaller values. This process is simple if one requires the boundaries to be smooth and one avoids examining the motion on a caustic. We have not been particularly concerned with the motion at or near caustics in this study since we are primarily interested in developing a methodology

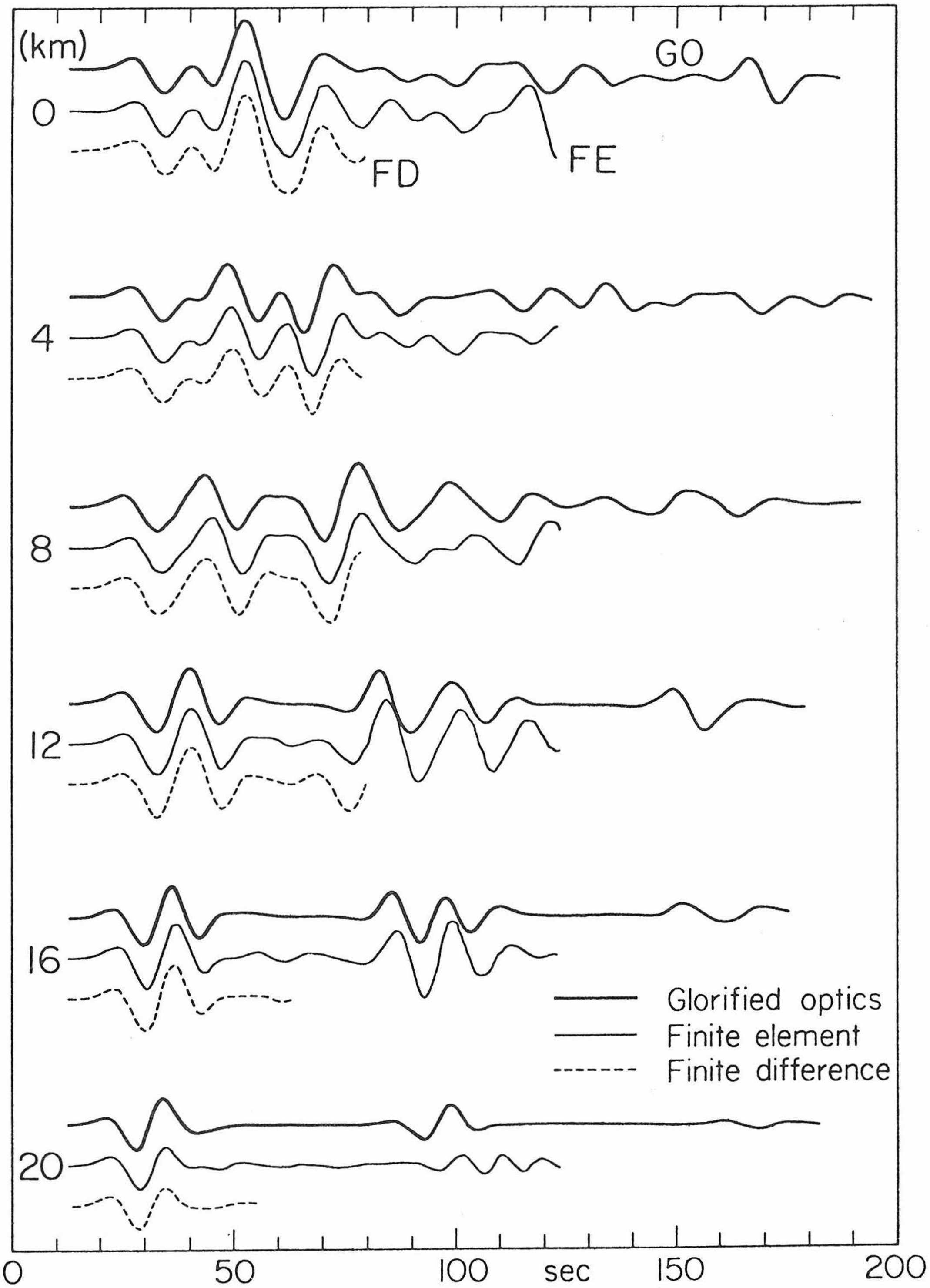

Figure 2.12 The comparison between the results of glorified optics, finite element, and finite difference. The later results were obtained from Larner (1970), Figure 4.9. The traces are the tangential displacement at surface receivers with horizontal distances of 0 to 20 km from the center of the basin.

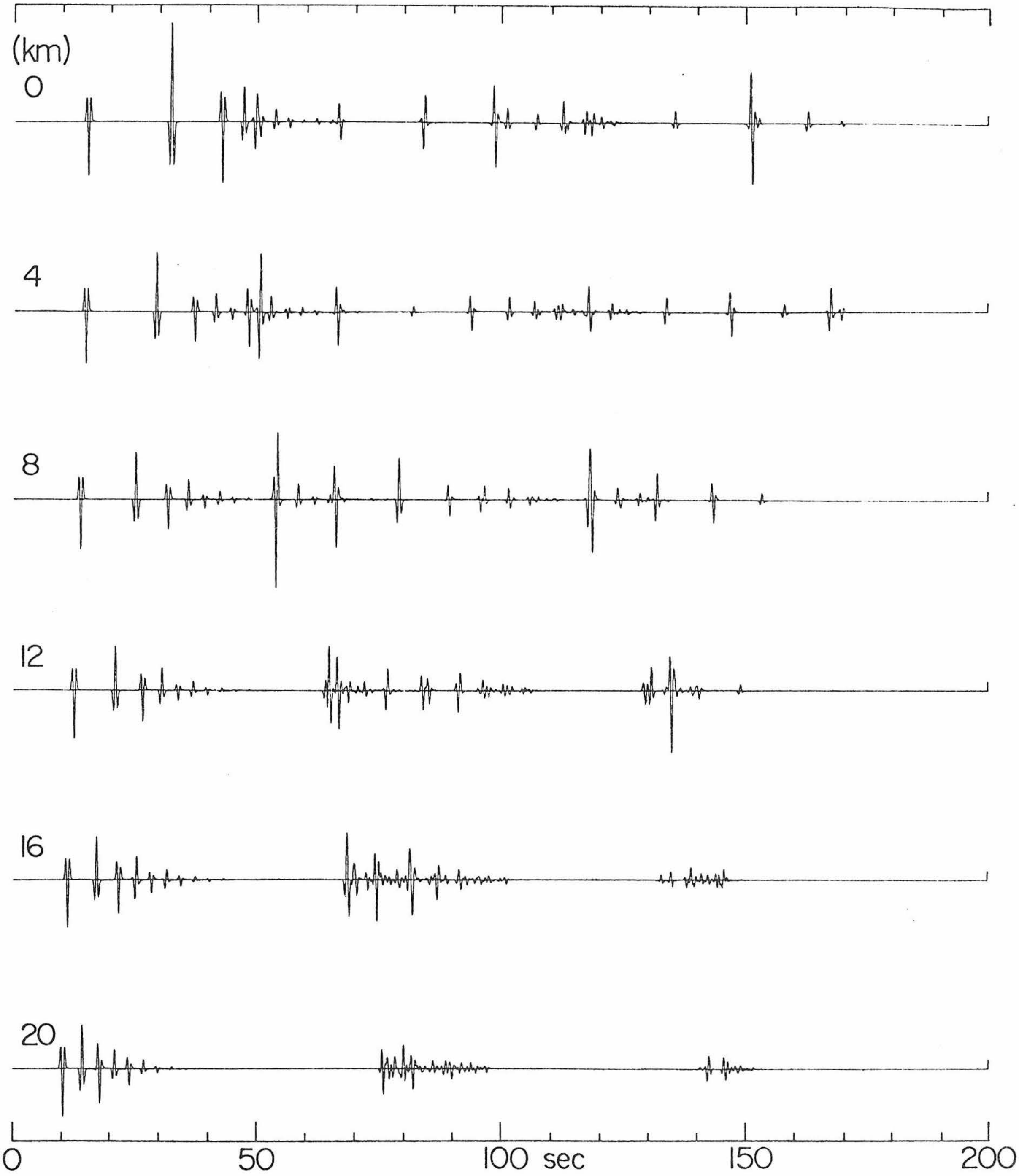

Figure 2.13 Diagram showing the SH displacement caused by vertically impinging plane wave with short pulse. The source time function is the Ricker's wavelet, see formula (2.26) with $T_p$ = 1 sec, $t_s$ = 1 sec.

for studying seismograms to infer the broad features of structure. On the other hand, the fine geometric detail needed to form caustics in regions of earthquake hazards abound and the role of such focusing could be highly significant.

In Figure 2.14a and 2.14b, we show the shape of the wavefront propagating in the basin. Along the caustics, we can see the wavefront is sharply bent. This effect can make the wavefront become extremely complicated as time goes on. We can see also that the wavefront at later stages includes two portions, one is propagating up and down, the other is propagating back and forth in the grazing direction.

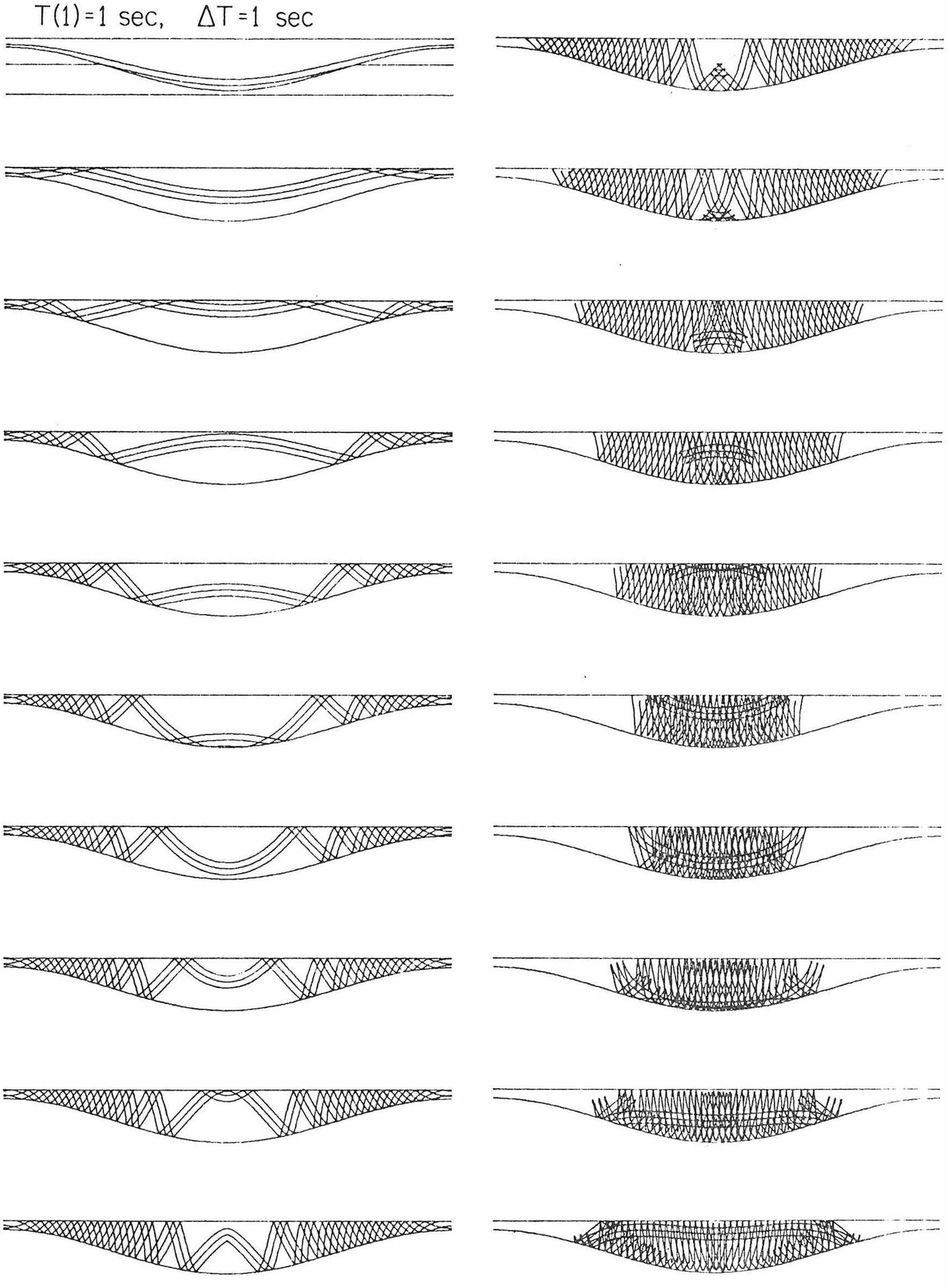

Figure 2.14a The shape of the propagating wavefront. T(1) is the starting time. Δt is the time step. In each plot, three traces corresponding to three time steps are drawn.

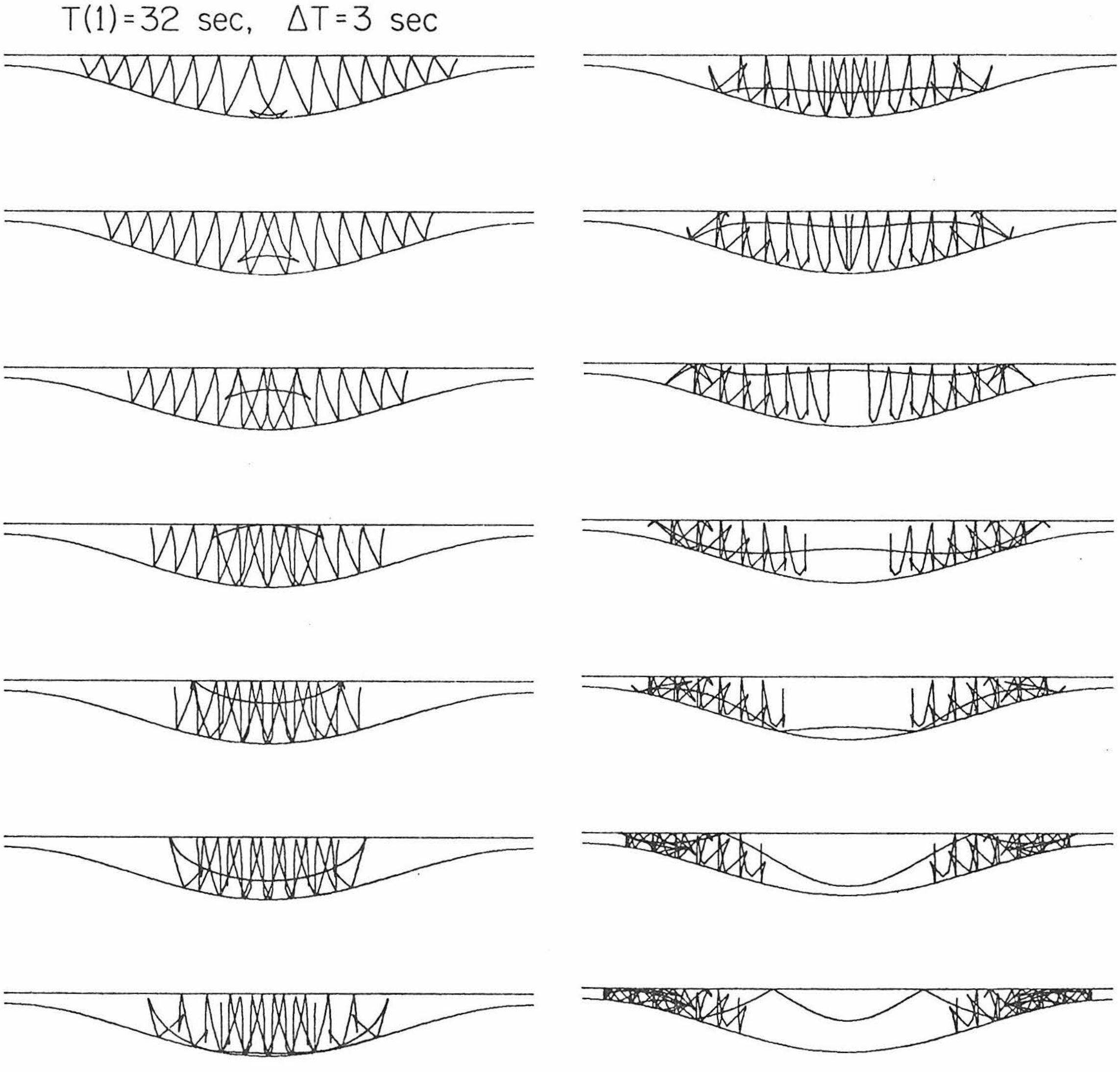

Figure 2.14b The shape of the propagating wavefront. T(1) and Δt have the same meaning as those in Figure 2.14a. In each plot only one trace is drawn so that we can examine the details.

# DISCUSSION

In general, curved boundaries introduce a number of interesting effects, namely frequency dependent reflection coefficients and geometrical focusing with the latter being the dominant feature in the basin study. The reason for this result is chiefly caused by the assumption of plane waves, constant p, where we essentially assume infinite travel time compared to the source duration. This assumption would appear to be appropriate for many seismological problems, some examples are the development of body wave codas and waveform complexity. The interpretation of recordings in terms of synthetics for these applications has been predicated almost exclusively on the simplifying assumption of flat layers. Given the experience developed in the basin study we feel it would be useful to briefly review these subjects.

Most observations of nuclear explosions made at distances between 30 and $90^{o}$ are quite simple, especially if the station is located on bedrock as noted by Thirlaway (1966). However, many records show a large complicated coda which has drawn much attention because of the use of P-wave complexity as a discriminant between earthquakes and explosions. An example of a simple and a rather complicated P-wave is given in Figure 2.15. Possible explanations have been put forth by numerous authors. Douglas et al. (1971) suggest that the direct P has been attenuated by passing through a lower Q zone relative to the later arrivals. Woodhouse (1973) suggests that strong later arrivals are diffracted arrivals from the upper mantle transition zones. More recent studies (Simpson and Cleary, 1977) suggest that P-signal complexity is caused by random scattering along the entire path. It

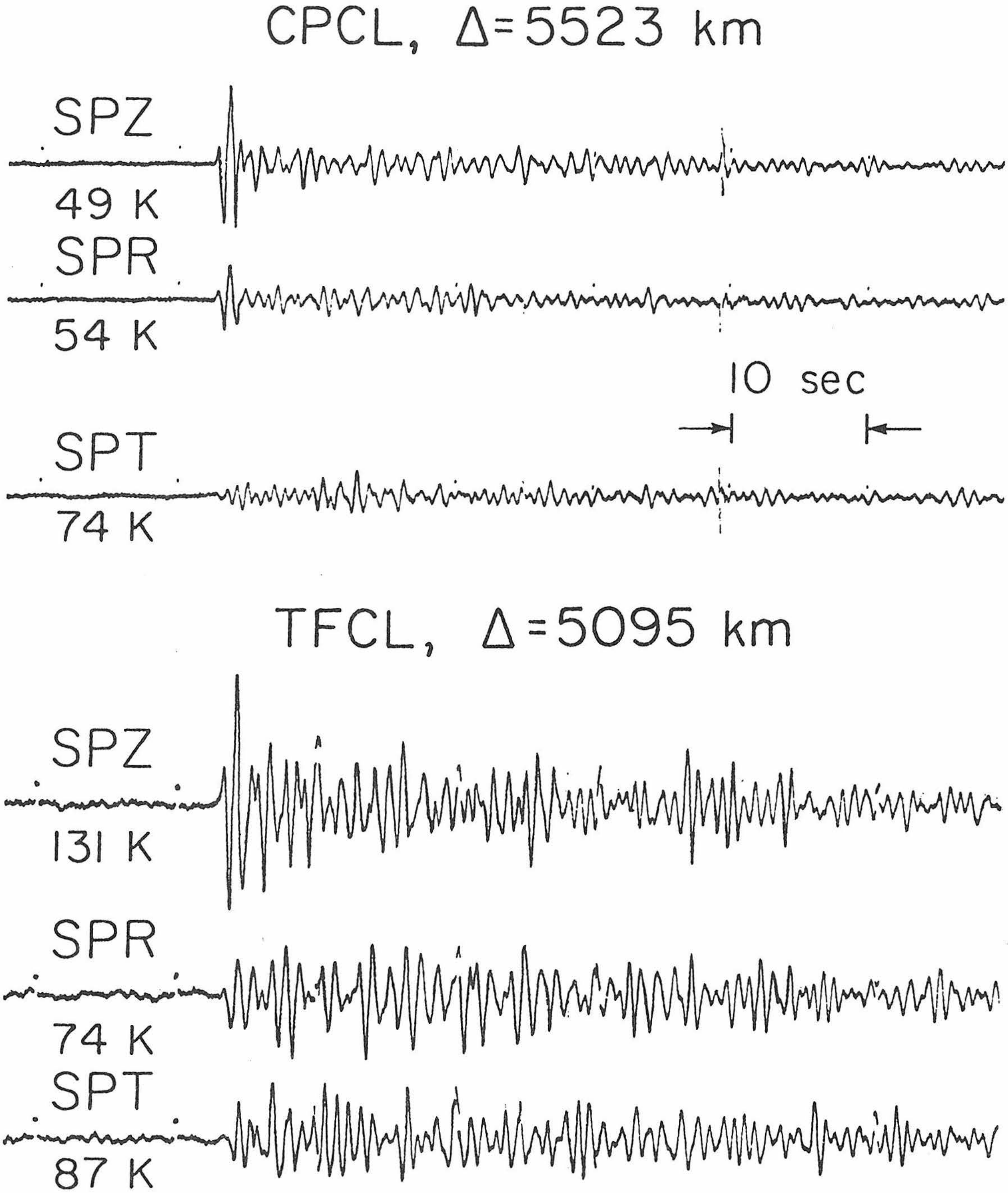

Figure 2.15 A comparison of the three components of observed motion of the Long Shot nuclear explosion at two sites in Southern California showing the P-wave complexity of TFCL (Taft) relative to CPCL (Campo).

would appear to us that the type of scattering discussed in this paper would be good explanation of the phenomena in that the scattering could come from shallow structure near the source (Figure 2.13 in reverse, using the reciprocity principle) and/or the receiver structure. For the example given in Figure 2.14, we would prefer the latter interpretation since these two stations are at nearly the same ray parameter. The station CPCL is setting on bedrock whereas TFCL is near the edge of the Great Valley. Our proposed technique appears ideally suited to study such problems.

Another application is with waveform complexity observed in refraction profiling, especially oceanic exploration with OBS receivers. It is common practice to drop OBS's in small basins of sediments to insure proper coupling to the bottom. However, in many such situations the OBS records are much more complicated than hydrophone recording near the surface of the ocean, see Lewis and McClair (1977). In this case, converted shear waves could easily become partially trapped and complicate the motion. To test this hypothesis would require a more complete data set. However, in general, the whole question about the intensity and waveform complexity in the presence of uneven bottom sedimentary cover could be handled with this technique.

Still another interesting application of this technique is with respect to site amplification effects observed in earthquake studies. There is abundant evidence of accelerations in excess of gravity occurring during earthquakes, see for example Morrill (1972). Numerous authors using numerical codes suggest that 25% of such high values can be attributed to topography effects, Boore, (1973), Trifunac (1971), or Bouchon (1973). However, it would appear to be quite easy to generate a factor of two by subsurface focusing at high frequencies of the type discussed in the previous section. But since the observations of large earthquakes contain information from 20 Hz to static offsets, we must be careful to understand the effects of lateral structure at all wavelengths. Thus, we have started work on including the effects of boundary curvature on curved wavefronts where the duration of signal need not be short compared to the travel time.

In summary, we have presented a practical method of generating synthetic seismograms for models containing non-parallel boundaries. The method consists of summing generalized rays describing the various possible paths based on the ray construction for dipping structure discussed earlier in Chapter 1. The response of each ray is determined by its numerical behavior near its particular arrival time. A comparison between synthetics generated by this new method with those obtained by finite element for a basin structure are presented and a number of possible applications discussed.

## REFERENCES

Aki, K. and K. L. Larner (1970). Surface motion of a layered medium having an irregular interface due to incident plane SH wave, J. Geophys. Res. 75, 933-954.

Boore, D. (1973). The effect of simple topography on seismic waves: implications for the accelerations recorded at Pacoima Dam, San Fernando Valley, California, Bull. Seism. Soc. Am. 63, 1603-1609.

Boore, D. M., K. L. Larner, and K. Aki (1971). Comparison of two independent methods for the solution of wave-scattering problems: Response of a sedimentary basin to vertically incident SH waves, J. Geophys. Res. 76, 558-569.

Bouchon, M. (1973). Effect of topography on surface motion, Bull. Seism. Soc. Amer. 63, 615-632.

Burdick, L. J. and G. R. Mellman (1976). Inversion of the body waves from the Borrego Mountain Earthquake to the source mechanism, Bull. Seism. Soc. Am. 66, 1485-1499.

Douglas, A., P. D. Marshall, and D. Corbishley (1971). Absorption and the complexity of P signals, Nature Phys. Sci. 232, 50-51.

Hill, D. P. (1974). Phase shift and pulse distortion in body waves due to internal caustics, Bull. Seism. Soc. Am. 64, 1733-1742.

Helmberger, D. V. (1968). The crust-mantle transition in the Bering Sea, Bull. Seism. Soc. Am. 58, 179-214.

Hong, T. L. and D. V. Helmberger (1977). Generalized ray theory for dipping structure, Bull. Seism. Soc. Am. 67, 995-1008.

Hong, T. L. and D. Kosloff (1978). An application of the finite element method in wave propagation problems involving irregular structures, submitted to Bull. Seism. Soc. Am.

Larner, K. L. (1970). Near-Receiver Scattering of Teleseismic Body Waves in Layered Crust-Mantle Models Having Irregular Interfaces, Thesis, Massachusetts Institute of Technology, Cambridge, MA.

Lewis, T. R. and J. McClair (1977). Problems with converted shear waves as seen by ocean bottom seismometers and surface buoys, Bull. Seism. Soc. Am., in press.

Morrill, B. J. (1972). The San Fernando, California, Earthquake of February 9, 1971, U.S. Geol. Survey Profess. Paper 733 22, 60-65.

Simpson, D. W. and J. R. Cleary (1977). P-signal complexity and upper mantle structure, Geophys. J. R. astr. Soc. 49, 747-756.

Thirlaway, H. I. S. (1966). Interpreting array records: Explosion and earthquake P wave trains which have traversed the deep mantle, Proc. R. Soc. London Acad. 290, 385-395.

Trifunac, M. D. (1971). Surface motion of a semi-cylindrical alluvial valley for incident plane SH waves, Bull. Seism. Soc. Am. 61, 1755-1770.

Woodhouse, J. H. (1973). Diffraction by anomalous regions in the Earth's mantle, Geophys. J. R. astr. Soc. 32, 295-324.

# APPENDIX

In order to help understanding, the derivation of (2.10) is as follows,

$$t = \sum_{m=1}^{3} (p_m d_m + \eta_m h_m)$$

$$\frac{d^2 t}{dp_1^2} = \frac{d}{dp_1}\left(\frac{dt}{dp_1}\right) = \frac{d}{dp_1}\left[\sum_{m=1}^{3}\left(d_m \frac{dp_m}{dp_1} - h_m \frac{p_m}{\eta_m}\frac{dp_m}{dp_1}\right)\right]$$

$$= \sum_{m=1}^{3}\left[\left(d_m - h_m \frac{p_m}{\eta_m}\right)\frac{d^2 p_m}{dp_1^2} - \frac{(\eta_m^2 + p_m^2)\, h_m}{\eta_m^3}\left(\frac{dp_m}{dp_1}\right)^2\right]$$

$$\frac{dp_m}{dp_1} = \frac{dp_m}{dp'_m}\,\frac{dp'_m}{dp_{m-1}}\,\frac{dp_{m-1}}{dp'_{m-1}} \cdots\cdots \frac{dp_2}{dp'_2}\,\frac{dp'_2}{dp_1}$$

$$= \frac{dp_m}{dp'_m}\,\frac{dp_{m-1}}{dp'_{m-1}} \cdots\cdots \frac{dp_2}{dp'_2}$$

where $p_m$ and $p'_m$ are the ray parameters of the m-th ray segment, associated respectively with the local coordinate systems suitable to describe the local boundary conditions at its two ends. Note that $p_{m-1} = p'_m$ by Snell's law.

$$\text{at } t = t_o, \quad p_m = \frac{\sin\theta_m}{v_m}, \quad p'_m = \frac{\sin\theta'_m}{v_m}$$

$$\eta_m = \frac{\cos\theta_m}{v_m}, \quad \eta'_m = \frac{\cos\theta'_m}{v_m}$$

where $v_m$ is the wave velocity of the medium.

$$\text{Also,} \quad d_m - h_m \cdot \frac{p_m}{\eta_m} = 0$$

Therefore,

$$\left(\frac{d^2t}{dp_1^2}\right)_{t=t_o} = \sum_{m=1}^{3}\left[\frac{-v_m h_m}{\cos^3\theta_m}\left(\frac{\cos\theta_m}{\cos\theta'_m}\,\frac{\cos\theta_{m-1}}{\cos\theta'_{m-1}}\cdots\cdots\frac{\cos\theta_2}{\cos\theta'_2}\right)^2\right]$$

$$= \sum_{m=1}^{3}\left[\frac{-v_m h_m}{\cos^3\theta_m}\,\frac{\cos^2\theta_m}{\cos^2\theta_1}\left(\frac{\cos\theta_{m-1}}{\cos\theta'_m}\,\frac{\cos\theta_{m-2}}{\cos\theta'_{m-1}}\cdots\frac{\cos\theta_1}{\cos\theta'_2}\right)^2\right]$$

$$= \sum_{m=1}^{3}\left[\frac{-v_m h_m}{\cos^3\theta_m}\,\frac{\cos^2\theta_m}{\cos^2\theta_1}\left(\frac{v_{m-1}d\theta'_m}{v_m d\theta_{m-1}}\,\frac{v_{m-2}d\theta'_{m-1}}{v_{m-1}d\theta_{m-2}}\cdots\frac{v_1 d\theta'_2}{v_2 d\theta_1}\right)\left(\frac{\cos\theta_{m-1}}{\cos\theta'_m}\,\frac{\cos\theta_{m-2}}{\cos\theta'_{m-1}}\cdots\frac{\cos\theta_1}{\cos\theta'_2}\right)\right]$$

$$= \sum_{m=1}^{3}\left[\frac{-R_m v_1}{\cos^2\theta_1}\,\frac{d\theta_m}{d\theta_1}\left(\frac{\cos\theta_{m-1}}{\cos\theta'_m}\,\frac{\cos\theta_{m-2}}{\cos\theta'_{m-1}}\cdots\frac{\cos\theta_1}{\cos\theta'_2}\right)\right]$$

We note that $d\theta_m = d\theta'_m$ since this quantity is invariant with respect to the rotation of coordinate system. Therefore,

$$\left[\eta_1\left|\frac{d^2t}{dp_1^2}\right|^{\frac{1}{2}}\right]_{t=t_o} = \frac{1}{\sqrt{v_1 d\theta_1}}\left[\sum_{m=1}^{3} R_m d\theta_m\left(\frac{\cos\theta_{m-1}}{\cos\theta'_m}\,\frac{\cos\theta_{m-2}}{\cos\theta'_{m-1}}\cdots\frac{\cos\theta_1}{\cos\theta'_2}\right)\right]^{\frac{1}{2}}$$

## Chapter 3

# AN APPLICATION OF THE FINITE ELEMENT METHOD IN WAVE PROPAGATION PROBLEMS INVOLVING IRREGULAR STRUCTURES

## ABSTRACT

The finite element method is very effective in solving problems involving wave propagation in irregular structure, especially since in most cases these problems do not have closed form solutions. This study presents a comparison between the finite element method and analytic solutions for two typical problems, namely, one of an SH pulse propagating through a dipping layer with a low shear velocity, and the other of a vertically incident SH wave impinging on a curved boundary separating two regions with contrasting wave velocities. The study is concerned with layer thicknesses of about 2-10 km, a time window of about 30-100 sec, and wave velocities between 1-4 km/sec. The results of the calculation are presented in the time domain and the resolution power of the finite element method is discussed. Some interesting characteristics of wave propagation in such structures are pointed out.

# INTRODUCTION

Seismology involves elastodynamics in a composite medium. Generally, rigorous analytical solutions are limited to problems involving regular structures which can be trivially described in a Cartesian, spherical or cylindrical coordinate system. However, irregular structures are such common features in the earth's crust that we can not go any further without understanding them. In the recent papers by Hong and Helmberger (1977, 1978), analytical methods for some of these problems are introduced. Since the accuracy of certain frequency-dependent approximations in their methods cannot be rigorously justified, an independent check is necessary. Finite element methods, as well as finite difference methods, are the best for this purpose. In addition, these methods have very high potential to be used as a general procedure to investigate many interesting problems in both seismology and earthquake engineering.

In this study, we used a low order, explicit scheme, which was originally developed by Frazier and Peterson (1974) and named as SWIS. It is a very fast scheme but needs dense grid to achieve accuracy. On the other hand, smaller element size requires smaller time steps to remain stable, thus costs more computing time. In the next section, we will discuss resolution power and stability, and find an efficient way to grid a system.

# RESOLUTION POWER AND STABILITY

The resolution power is the ability of a scheme to resolve signal from noise. It can be achieved if the dominant modes in source field are well sampled. The criterion varies from one scheme to another Here, we took a severe consideration to keep the grid size smaller than one-tenth of the quarter-power wavelength. The quarter-power wavelength is defined to be the wavelength corresponding to the frequency of upper-quarter-power point in the power spectrum of the source time function. Generally, similar criterion of resolution power should also be considered in time domain. But in an explicit scheme, it is not necessary since stability requirements also insure that the time steps are sufficiently small.

In many time stepping schemes, certain modes can be amplified step by step and rapidly ruin anything else. The stability criterion of the three-step central difference scheme, used in SWIS, is $\pi f \Delta t \leq 1$ ,where f is the frequency of a mode, $\Delta t$ is the time step. The highest possible mode in the system is determined by the grid size. If we take the most severe consideration, the highest mode could be the one with frequency of $(v_s/2h_s)$ , where $h_s$ is the minimum grid size in the region of highest wave velocity, $v_s$. Therefore the time step $\Delta t$ should be smaller than $2h_s/\pi v_s$.

# CASE STUDY

Here we are going to investigate some cases which are interesting in geophysics and on which some analytical methods have been worked out. We classify these cases into A) and B).

## A) SH-wave Propagation in a Dipping Layer Over a Half-space From a Uniform Line Source.

The structure we consider here is the same as that shown in Figure 1.8, with the following parameters, $\alpha = 10^{\circ}$, $L_1 = 2.24$ km, $L_2 = 9.47$ km, $L_3 = 4$ km, $L_4 = 10$ km, $L_5 = 31$ km, $\beta_1 = 1.6$ km/sec, $\beta_2 = 4.8$ km/sec, $\rho_1 = 2.6$ gm/cm$^3$, $\rho_2 = 2.7$ gm/cm$^3$. The grid system used in our computation is shown in Figure 3.1. Notice that quite a few distorted elements are introduced. Such a grid design is based on the consideration of compromising the requirements for accuracy and for computing economy. The maximum and minimum values of grid size, which control the resolution power and stability respectively, are:

In the region with $x \geq -20$ km,

$h_{max}$ (in layer) = 0.5 km, $h_{min}$ (in layer) = 0.42 km

$h_{max}$ (in half-space) = 1.5 km, $h_{min}$ (in half-space) = 0.40 km;

In the region with $x < -20$ km,

$h_{max}$ (in layer) = 1.5 km $h_{min}$ (in layer) = 0.42 km

$h_{max}$ (in half-space) = 4.5 km $h_{min}$ (in half-space) = 0.40 km.

The source time function is an equilateral triangle with duration of 3 seconds and peak value of 1. The corresponding quarter-power

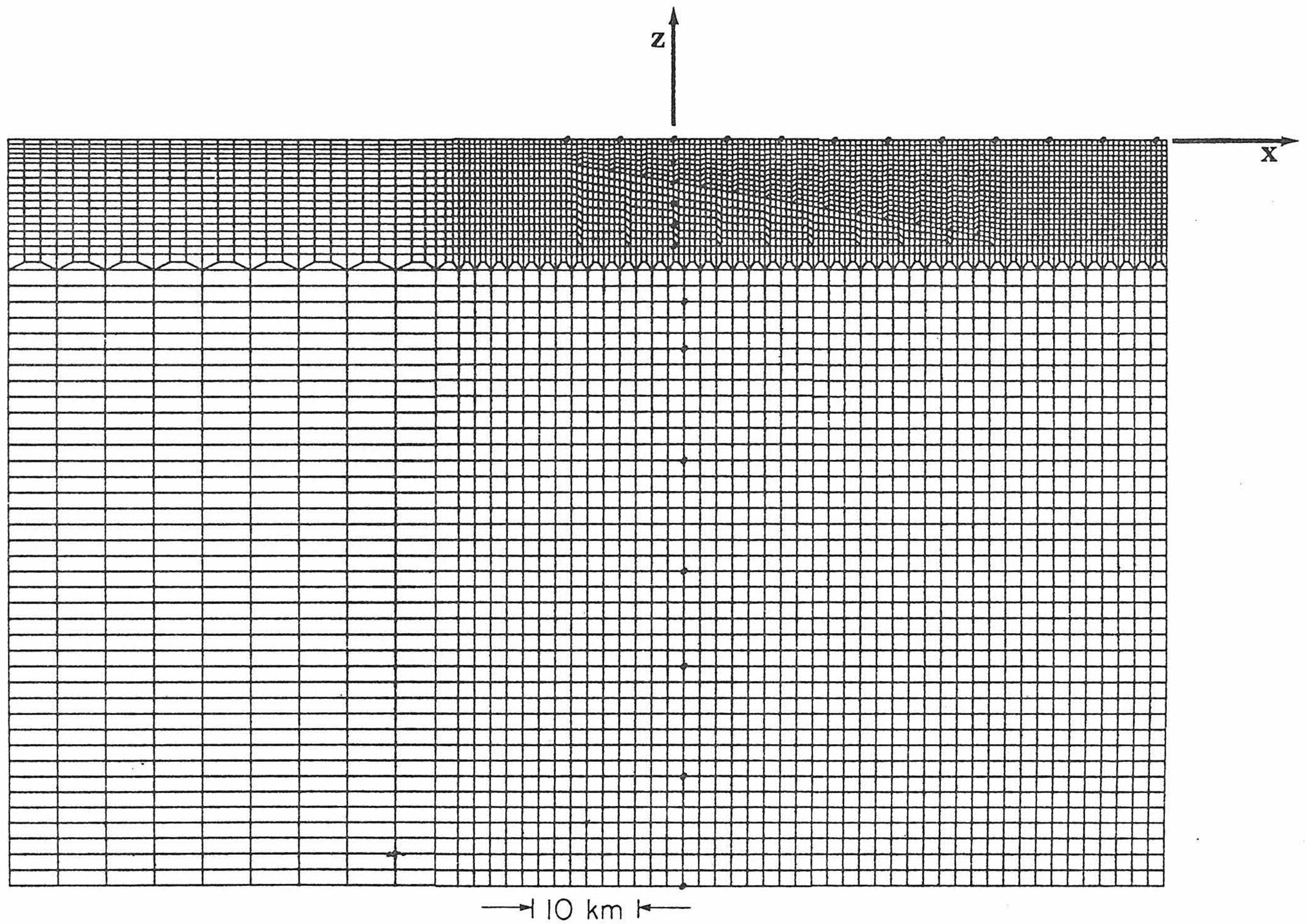

Figure 3.1 The configuration and grid system for the structure of a dipping layer over a half-space.

wavelength is 5.41 km in the layer and 16.22 km in the half-space. It is loaded at the node with coordinates $(x,z) = (0, -6.\text{ km})$. Notice that the criterion of resolution power is satisfied in the region with $x \geq -20$ km. However, in the region with $x \leq -20$ km, which is added to prevent the artificial reflections, the criterion is not satisfied. A source of concern is whether the noise generated there could interfere with the signal in the right region or not. Here we perform a test as follows. The medium in the layer is set to be identical to that in the half-space. The results are shown in Figure 3.2. If there are significant noises coming back from the left region, their arriving time at the two receivers separated by 20 km should be different. But there is no such phase that can be identified. Notice that the noises in Figure 3.2-a and Figure 3.2-b are not precisely reflecting the characteristics of noises in the real situation in which the shear velocity in the layer is smaller. However in Figure 3.2-c, we try to illustrate an equivalent situation by picking a location in the region where the ratio of grid size to quarter-power wavelength is larger.

After this test, we run the actual problem with the soft layer, described above. The results are shown in Figure 3.3. Notice that the rays transmitted from the half-space can be trapped in the dipping layer. We can pick the second phase of each trace in Figure 3.3 to examine it. It is apparent that this phase is gaining the feature of critical reflection at receivers away from the source in the down-dip direction. More detailed discussions through the generalized rays can be seen in Chapter 1. In Figure 3.3, the results of

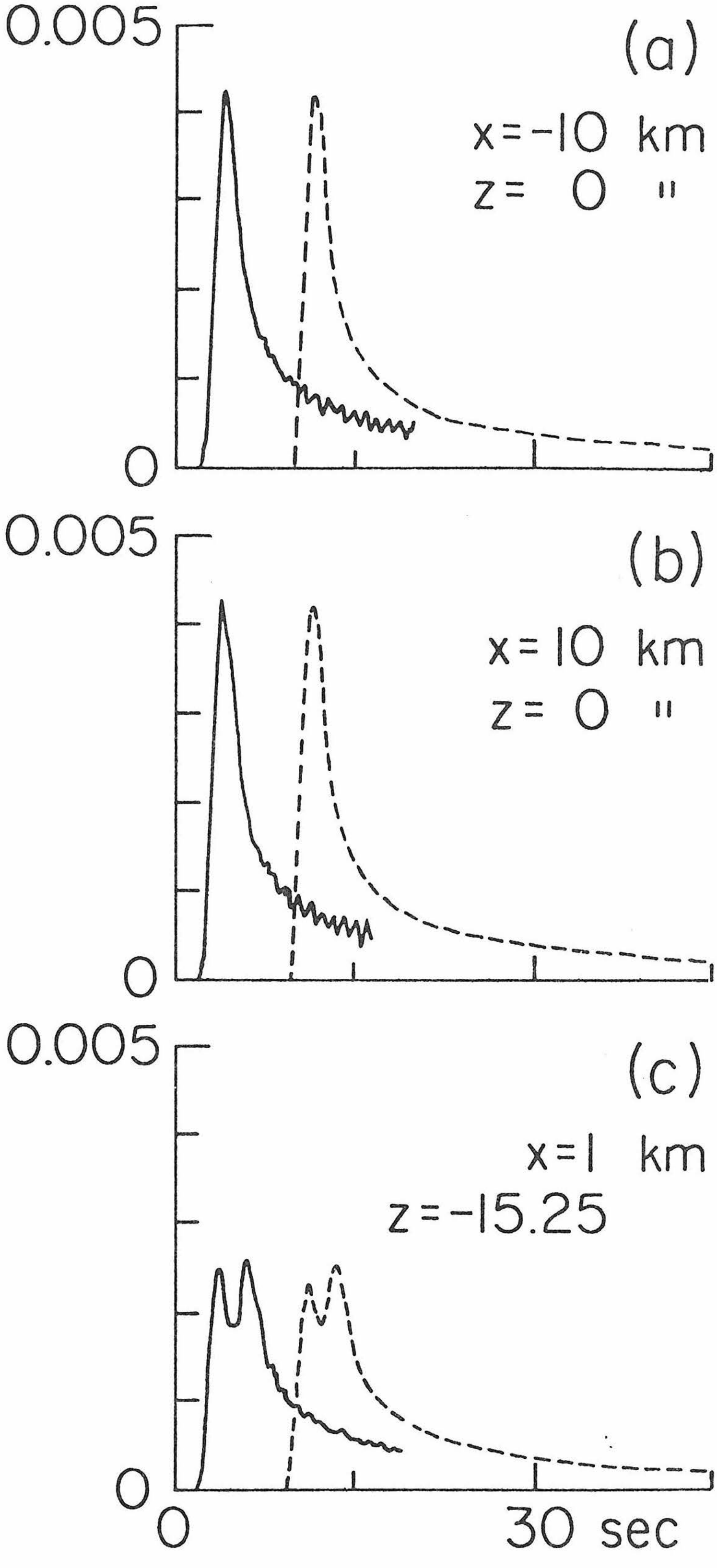

Figure 3.2 The displacements caused by an SH line source in a uniform medium gridded in the way shown in Figure 3.1. Analytical solutions are also presented for comparison.

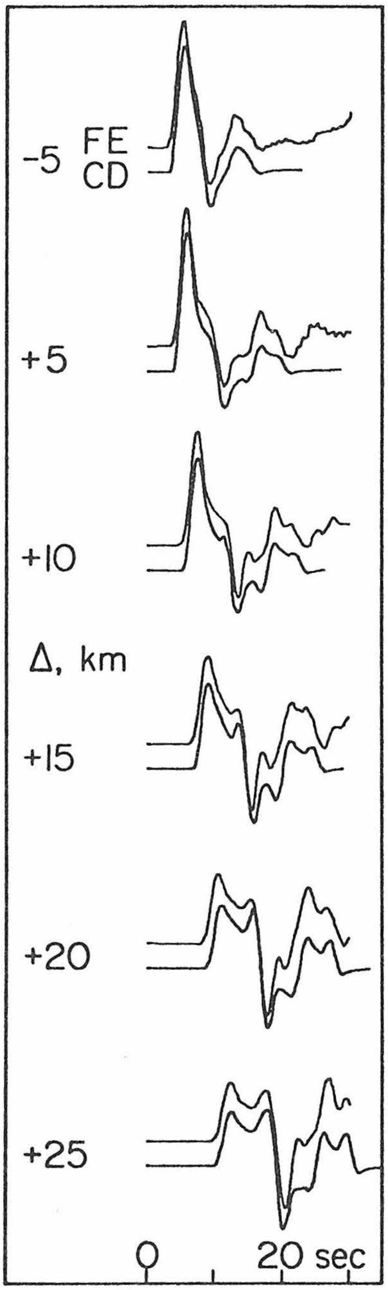

Figure 3.3 The displacements in a soft dipping layer caused by an SH line source. Analytical solutions, marked with CD, are also shown. Each number in this figure refers to the horizontal distance from source to each receiver which is on the surface.

generalized ray theory are also presented for comparison. The agreement is good in general. The long period drift found in this comparison should be due to the inaccuracy in the approximations pointed out in Chapter 1.

## B) The Interaction of an Incident Plane SH Wave With Structures Involving Curved Interfaces.

An incident plane SH wave with a given displacement time function f(t) can be simulated by loading body force on a plane with time function of df/dt. The reason is given in the Appendix.

(1) We consider the structure of two half spaces seperated by a periodic semicircular interface. For SH wave propagation,this structure is mathematically equivalent to a finite structure consisting of one period of the original structure with traction free boundaries at the sides. The configuration and the grid system are shown in Figure 3.4. The maximum and minimum values of the grid size are listed as follows,

$h_{max}$(in upper half-space) = 0.67 km, $h_{min}$(in upper half-space)=0.33 km
$h_{max}$(in lower half-space) = 2. km, $h_{min}$(in lower half-space)=0.33 km

In the upper half-space, the shear velocity is 1 km/sec and the density is 1 $gm/cm^3$. In the lower half-space, the shear velocity is 3 km/sec and the density is 1 $gm/cm^3$.

The source time function is an equilateral triangle with duration of 6 sec and peak value of 1. The corresponding quarter-power wavelength is 6.76 km in the upper half-space and 20.27 km in the lower

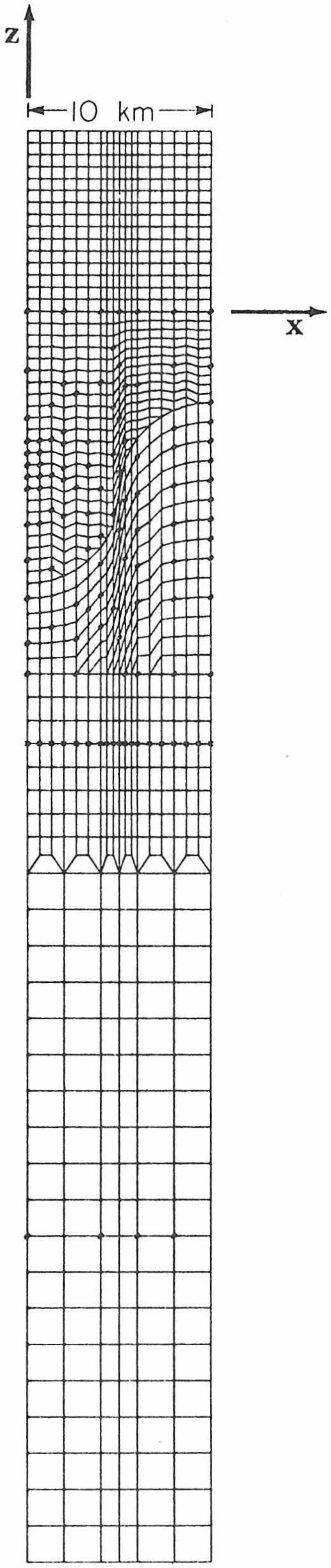

Figure 3.4 The configuration and grid system for the structure of two half-spaces separated by a semi-circular interface.

half-space. The source is loaded at nodes with z = -23.86 km.

in order to check how well this planar loading can simulate the teleseismic incidence, we perform the following test. The medium in the upper half-space is set to be identical to that in the lower half-space. Figure 3.5 shows the results, compared with analytical solution. The agreement can not be better.

Then we go back to the problem with soft upper half-space, Figure 2.6 shows the displacements at two locations in upper half-space. We would like to point out that the humps in those traces are indicating the arrival of some rays which experienced ninety degree phase shift by the effect of boundary curvature. The results of glorified optics, and of finite element method have been presented in Figure 2.6 for comparison. Notice that the long period components are not favored by glorified optics , even though we can still see good agreement in this comparison.

(2) We consider a soft basin over a half-space. In order to compare with Boore's results by finite difference method, we use the same model described below.

The equation of the interface is given by,

$$z(x) = \begin{cases} -D - \frac{C}{2}\left\{1-\cos\left[\frac{2\pi(x-w/2)}{w}\right]\right\}, & \text{for } -\frac{w}{2} \le x \le \frac{w}{2} \\ -D, & \text{elsewhere} \end{cases}$$

where, D = 1 km

w = 50 km

C = 5 km

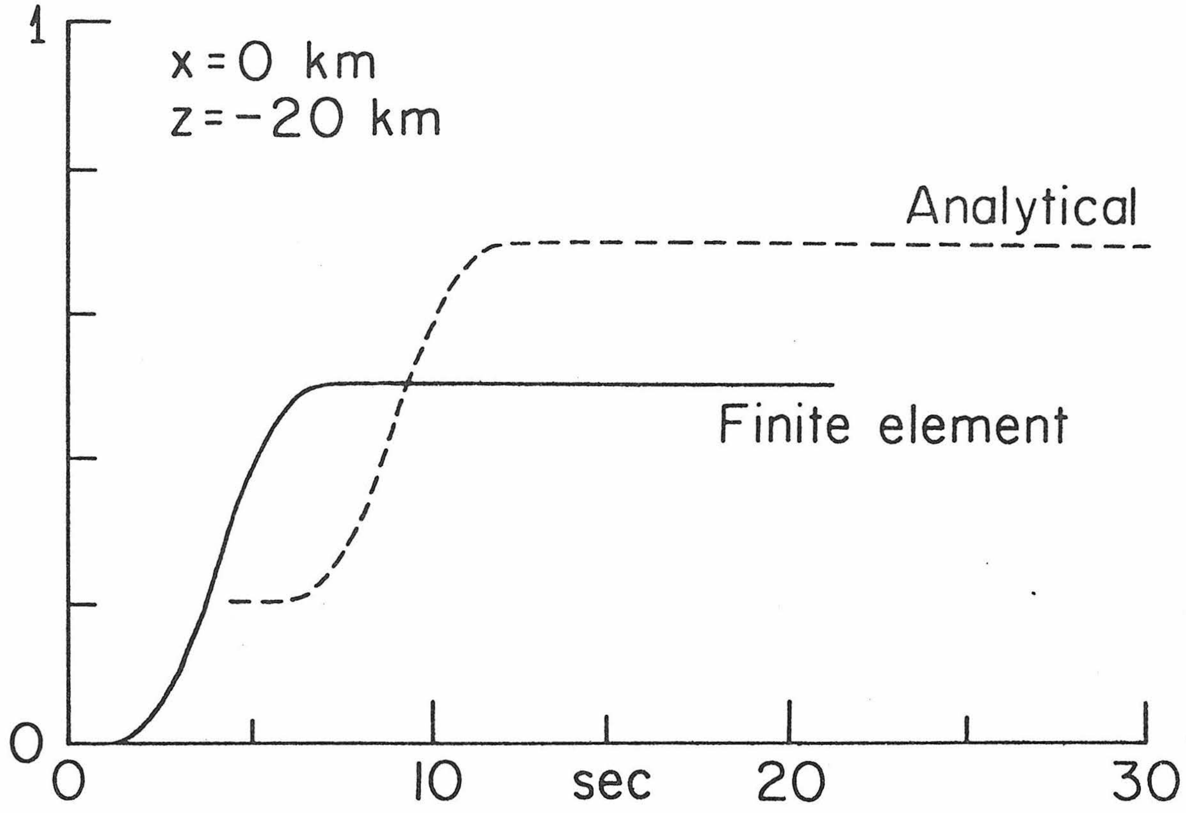

Figure 3.5 The displacement caused by a planar loading in a uniform medium gridded in the way shown in Figure 3.4.

In the layer, the shear velocity is 0.7 km/sec and the density is 2 gm/cm$^3$. In the half-space, the shear velocity is 3.5 km/sec and the density is 3.3 gm/cm$^3$.

A plane wave is impinging vertically with the displacement function f(t), the Ricker's wavelet :

$$f(t) = \frac{\sqrt{\pi}}{2} (a - \frac{1}{2}) \exp(-a)$$

and

$$a = 6(t - t_s)^2/(T_p \cdot \frac{\sqrt{6}}{\pi})$$

$t_p$ = 18.3 sec, $t_s$ is the time shift, can be given arbitrarily.

The configuration and grid system used in our computation is shown in Figure 3.6. The maximum and minimum values of grid size are listed as follows,

$h_{max}$ (in layer) = 0.71 km, $h_{min}$ (in layer) = 0.49 km

$h_{max}$ (in half-space) = 3.57 km, $h_{min}$ (in half-space) = 0.71 km

Nodal forces are loaded at the nodes with z = -19.8 km. The source time function, df(t)/dt, is drawn in Figure 3.7. The corresponding quarter-power wavelength is 6.90 km in the layer and 34.48 km in the half space.

The displacement at the surface receivers has been shown in Figure 2.12, accompanied with the results of glorified optics. We noticed that a simple plane wave pulse becomes a long wave train after interacting with the soft basin, and its shape is varying dramatically from one location to another. At the central part of the basin, the displacement can be much stronger than we can ever expect in the

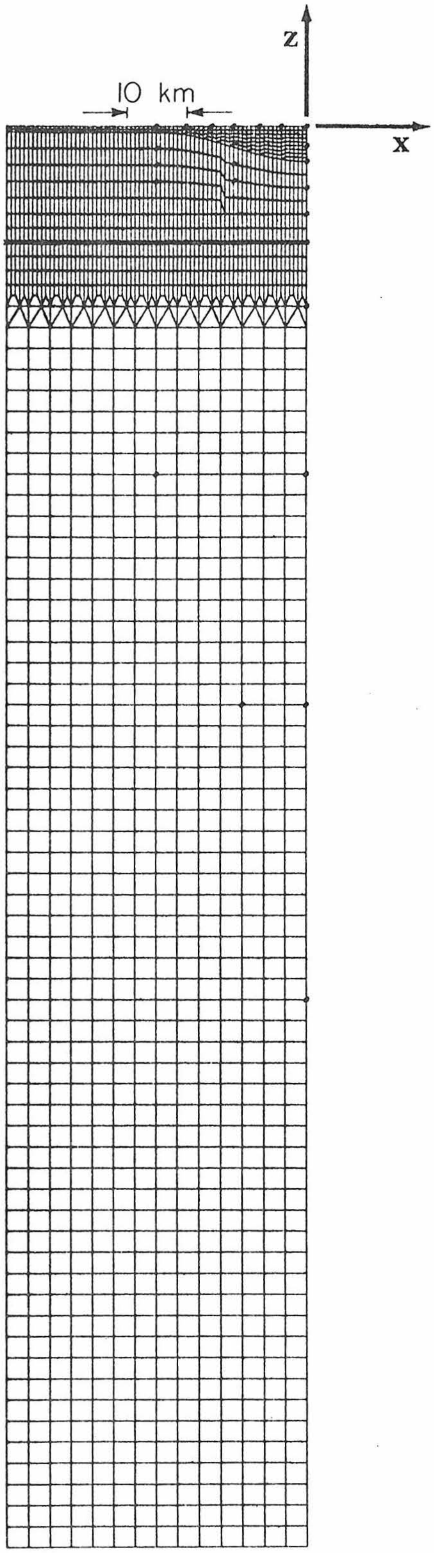

Figure 3.6 The configuration and grid system of a basin structure.

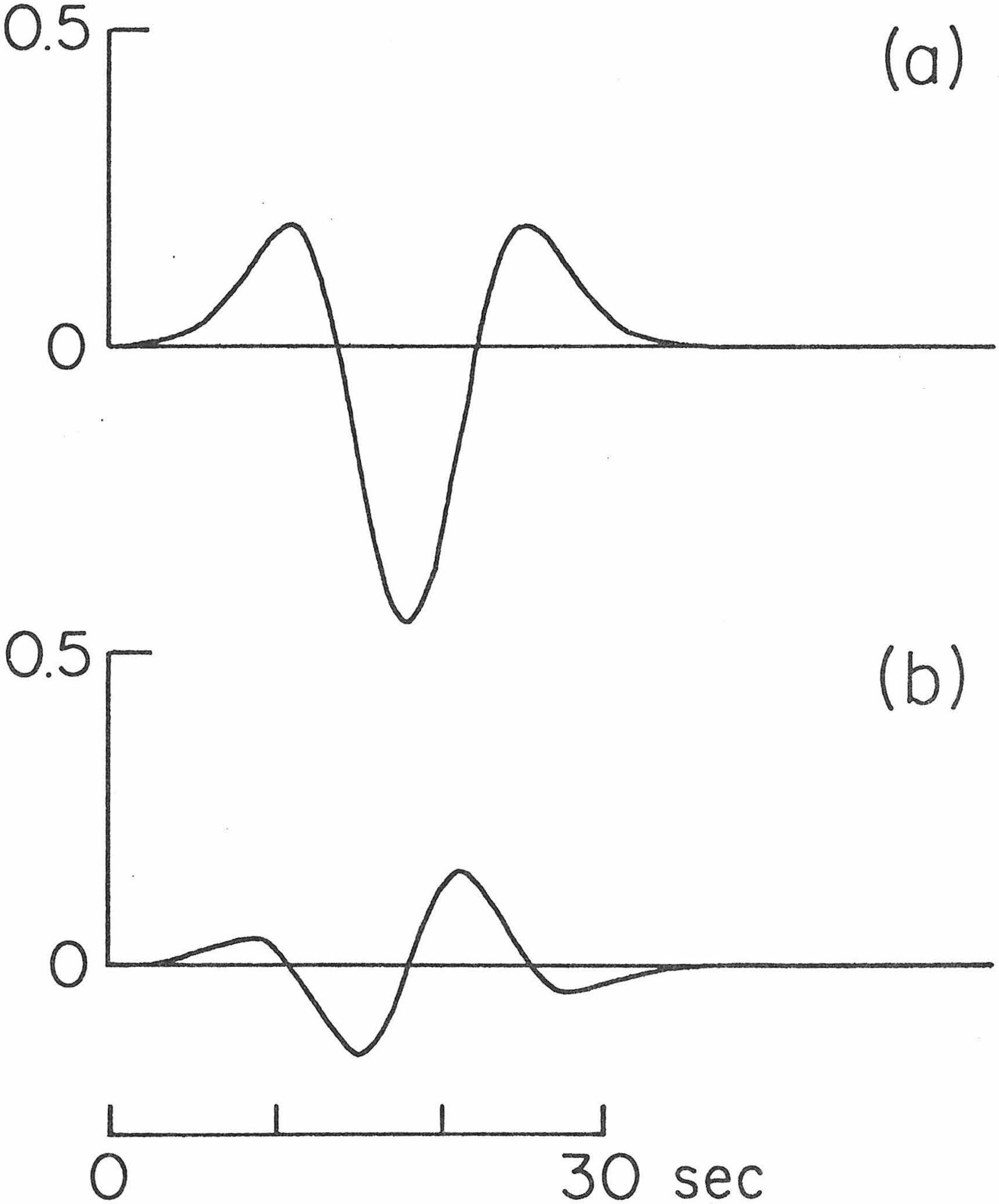

Figure 3.7 The Ricker's wavelet (a) and its derivative (b).

structures with planar interfaces. And at a location close to the edge of the basin, the wave train shows the separation of two groups of phases, one of them comes across the basin from the other side. The complete interpretation about what these phases are and why they gain large amplitude has been given in Chapter 2.

From Figure 2.12, we can see the agreement is good in general. Certain disagreements show up. We think that is caused by the inaccuracy in glorified optics. In Figure 3.8, we present the spatial deformation pattern of the soft basin, varying from time to time. We can see that the energy trapped in the basin can hardly get out. Thus the vibration lasts very long, especially in the central part of the basin.

## DISCUSSION

In regular structures, uniform grid system with elements of regular shape can be trivially made. However, in irregular structure, we have to introduce many distorted elements.

The stiffness or restoring force evaluated in a distorted element is less accurate. However, through the comparisons with analytical solutions in this study, there is no evidence that such inaccuracy could significantly distort the major part of a signal, as long as the criterion of resolution power is satisfied.

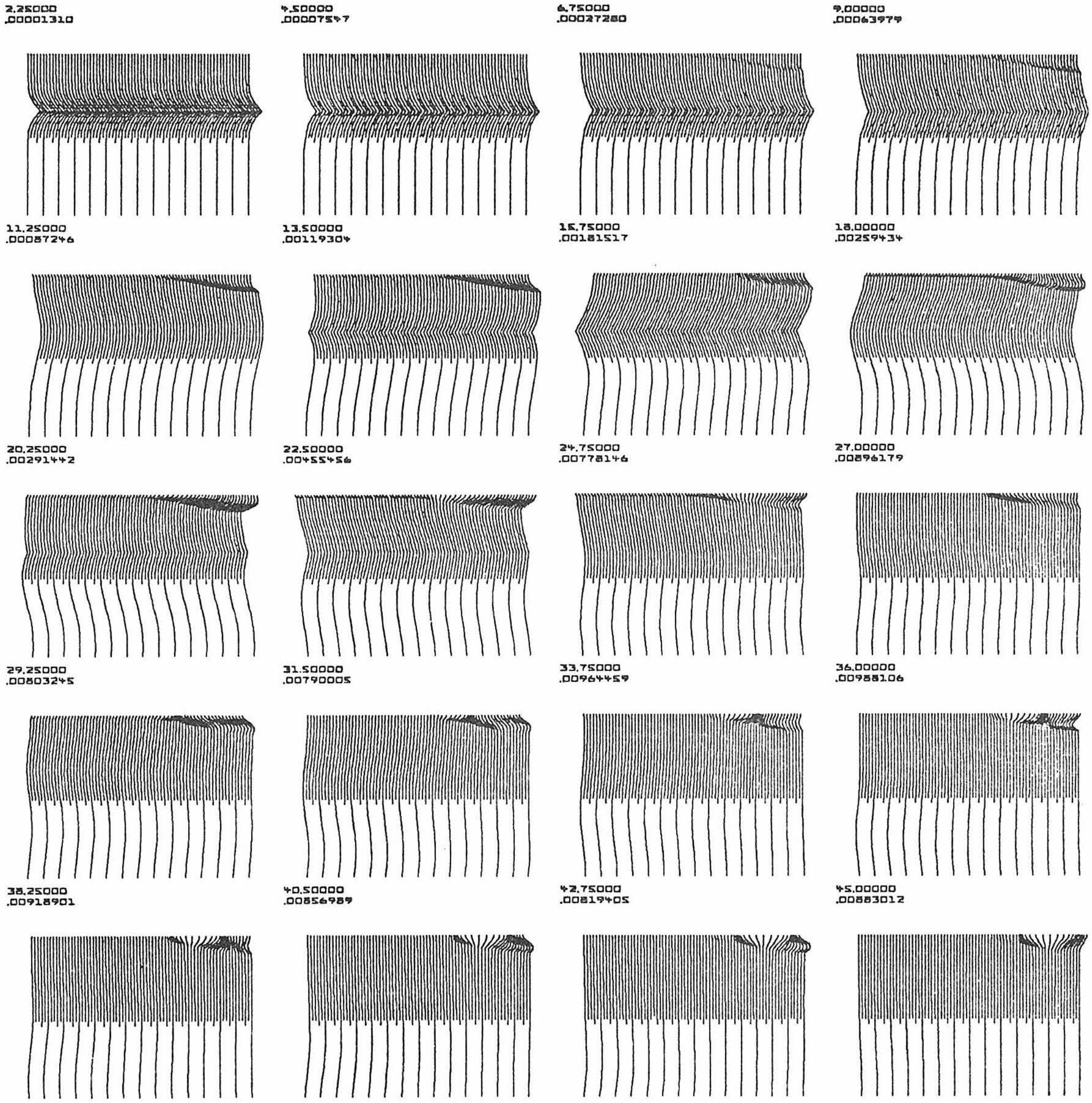

Figure 3.8a The spatial deformation pattern from time to time, At the upper left corner of each plot, there are two numbers. The upper one indicates the time in seconds, the lower one indicates the maximum value of the deformation at that moment. Notice that the SH displacement is drawn in the x-direction.

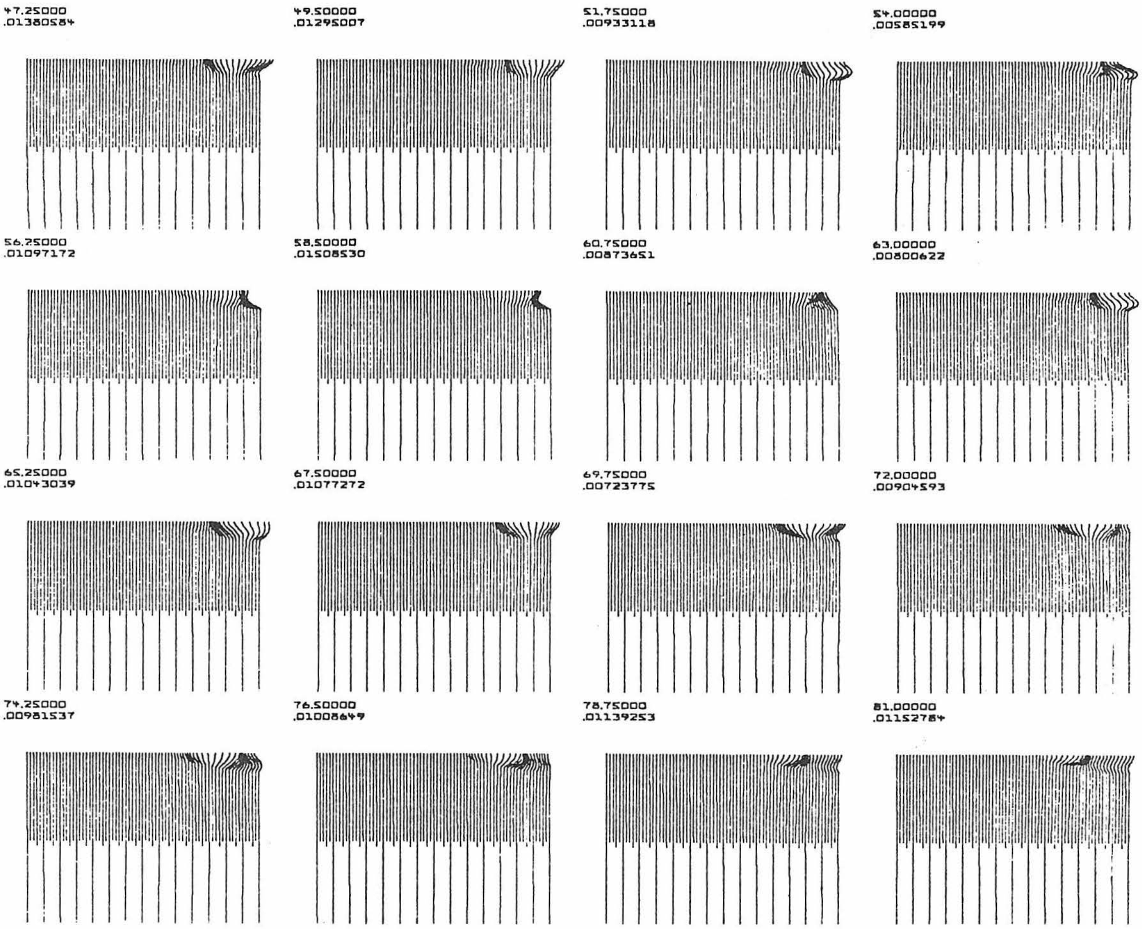

Figure 3.8b Continuation of Figure 3.8a.

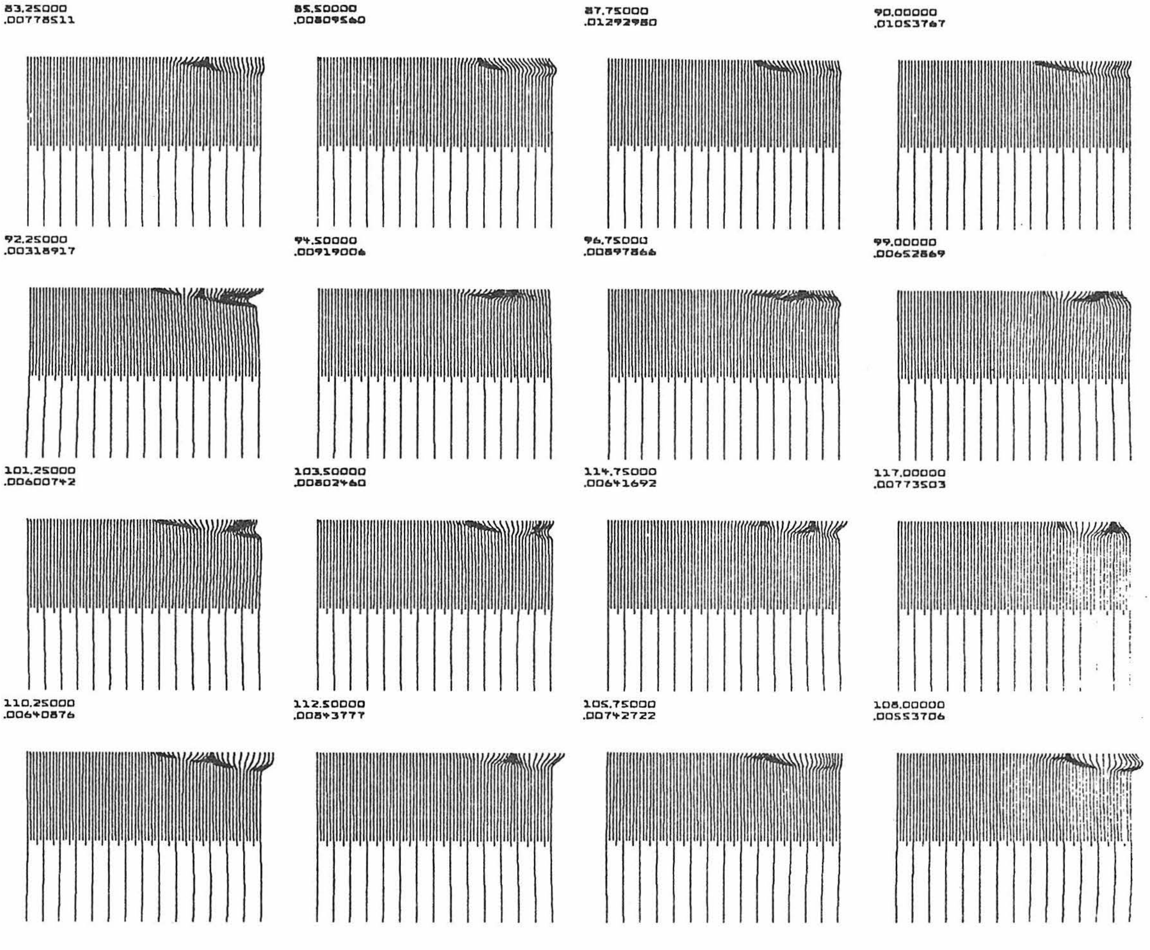

Figure 3.8c Continuation of Figure 3.8b.

# CONCLUSION

Although it is a powerful tool, the finite element method hasn't been used extensively in seismic modelling or inversion. One reason is, of course, the speed and cost of the existing computers. The other reason is, as other numerical methods, the connection of each phase in the synthetic seismogram with the structure parameters is implicit. In this paper, it is shown that by combining with the analytical approximation we can thoroughly understand the wave propagation in many irregular structures. And, thus seismic modelling and inversion to great details of the structures are possible.

# REFERENCES

Alford, R. M., K. R. Kelly, and D. M. Boore (1974). Accuracy of finite-difference modeling of the acoustic wave equation, Geophysics 39, no. 6, 834-842.

Boore, D. M., K. L. Larner, and K. Aki (1971). Comparison of two independent methods for the solution of wave-scattering problems: Response of a sedimentary basin to vertically incident SH waves. J. Geophys. Res. 76, 558-569.

Frazier, G. A., and C. M. Petersen (1974). Three-dimensional stress wave code for Illiac IV, Systems Science and Software, P. O. Box 1620, La Jolla, California, 92037.

Gallagher, R. H. (1975). Finite Element Analysis, Fundamentals, Prentice Hall, Inc., New Jersey.

Hong, T. L. and D. V. Helmberger (1977). Generalized ray theory for dipping structure, Bull. Seism. Soc. Am. 67, 995-1008.

Hong, T. L. and D. V. Helmberger (1978). Glorified optics and wave propagation in non-planar structure, submitted to Bull. Seism. Soc. Am.

Kosloff, D. D., and G. A. Frazier (1977). Treatment of hourglass modes in low order finite element codes, Intl. J. of Num. and Analytical Meth. in Geomechanics, in press.

Larner, K. L. (1970). Near-receiver scattering of teleseismic body waves in layered crust-mantle models having irregular interfaces, thesis, M.I.T., Cambridge, Mass.

# APPENDIX

The tests of grid systems are often performed in uniform media. Therefore, we list here the analytical solutions for calibrations.

In a whole-space, the differential equation of motion for SH-wave is

$$\rho\ddot{u} = \mu\left(\frac{\partial^2 u}{\partial x^2} + \frac{\partial^2 u}{\partial z^2}\right) + f(x,z,t)$$

here, u, the displacement in y-direction

x,y,z, Cartesian coordinates

f, the body force per unit volume

$\rho$, the density

$\mu$, the shear modulus

1) Line source, i.e.,

$$f(x,z,t) = \delta(x)\delta(z)\tau(t)$$

here, $\tau$, source time function

$\delta$, $\delta$-function

The solution is,

$$u(x,z,t) = \frac{1}{2\pi\mu}\left\{\tau(t) * \frac{1}{\sqrt{t^2-t_o^2}}\right\}, \quad t_o \equiv \frac{\sqrt{x^2+z^2}}{c}$$

here, $*$, means convolution

c, shear velocity

2) Planar loading, i.e.,

$$f(z,t) = \delta(z)\tau(t)$$

The solution is,

$$u(z,t) = \frac{c}{2\mu}\int_{o}^{t-t_o} \tau(\xi)\,d\xi \quad , \quad t_o = \frac{z}{c}$$